

Coherent super- and subradiant dynamics between distant optical quantum emitters

Alexey Tiranov^{†, 1,*} Vasiliki Angelopoulou,^{1,*} Cornelis Jacobus van Diepen,¹ Björn Schrinski,¹ Oliver August Dall’Alba Sandberg,¹ Ying Wang,¹ Leonardo Midolo,¹ Sven Scholz,² Andreas Dirk Wieck,² Arne Ludwig,² Anders Søndberg Sørensen,¹ and Peter Lodahl^{1, †}

¹Center for Hybrid Quantum Networks (Hy-Q), The Niels Bohr

Institute, University of Copenhagen, DK-2100 Copenhagen Ø, Denmark

²Lehrstuhl für Angewandte Festkörperphysik, Ruhr-Universität Bochum, Universitätsstraße 150, D-44801 Bochum, Germany

(Dated: October 6, 2022)

Photon emission is the hallmark of light-matter interaction and the foundation of photonic quantum science, enabling advanced sources for quantum communication and computing [1, 2]. While single emitter radiation can be tailored by the photonic environment [3], the introduction of multiple emitters fundamentally extends this picture [4, 5] following a “*more is different*” dictum [6]. The emerging collective effects include modified emission [7–10] and the creation of emitter-emitter entanglement [11], towards a new domain of strongly correlated light-matter quantum many-body physics [12, 13]. A fundamental challenge is that the radiative dipole-dipole coupling rapidly decays with spatial separation, i.e. within a fraction of the optical wavelength. This limitation can be overcome in waveguide QED where the coupling is ideally of infinite range [14, 15]. Here we realize distant dipole-dipole radiative coupling with multiple solid-state optical quantum emitters embedded in nanophotonic waveguides. We dynamically probe the collective response and identify both super- and subradiant emission as well as means to control the dynamics by proper excitation techniques. Subradiant states are particularly challenging to realize being highly sensitive to imperfections and decoherence. Our work constitutes a foundational step towards multi-emitter applications of technological importance, e.g., for realizing quantum transduction between microwave qubits and the optical domain [16] or for quantum memories with exponential improvement in photon storage fidelity [17].

Photon-mediated interaction between distant quantum emitters is opening new avenues in quantum information processing both in the optical [7, 8, 10, 11] and microwave domains [9]. In microwave QED, multi-qubit interactions have been studied [18, 19] and subradiant collective states coherently controlled [20]. Realizing such functionalities in the optical domain is significant: optical photons can be highly integrated, rapidly processed on-chip, and transmitted over extended distances [1, 2], making photonics the backbone technology for the quantum internet [21].

Coherent dipole-dipole interaction leads to the formation of collective emitter states featuring super- or subradiant decay rates [22], as controlled by the optical phase lag between the two emitters, cf. FIG. 1(a) for an illustration. Observation of collective emission requires a highly coherent light-matter interface. In particular, long-lived subradiant features may be elusive in the presence of experimental imperfections such as dephasing [23]. Previous reports in the optical domain include projective preparation of superradiant states as revealed in two-photon correlation measurements [24–27] that does not require photon-mediated emitter-emitter coupling. Spectroscopic evidence for coherent coupling was reported with for closely spaced dye molecules in a bulk medium [10, 28] or for vacancy center in a cavity [11]. Dynamical measurements of modified collective

emission would constitute direct experimental proof of coherent coupling and open new avenues towards applications. We report on the first observation of coherent dynamics of distant quantum dot (QD) emitters coupled via a photonic crystal waveguide (PCW) (see FIG. 1a) by observing both enhanced (superradiant) and suppressed (subradiant) dynamics of the photons emitted from the “waveguide-bonded QD molecule”. The QDs are brought into mutual resonance by Zeeman-tuning with a magnetic field. The coherent oscillations of the collective state are directly observed and found to be controllable by spectrally tuning the QDs and by varying the excitation conditions.

The coupled QDs are described by the effective Hamiltonian \mathcal{H}_{eff} (frame rotating at the excitation field frequency and $\hbar = 1$) [17, 29]

$$\sum_{m,n=1}^2 \left(J_{mn} - i \frac{\Gamma_{mn}}{2} \right) \sigma_n^+ \sigma_m^- + \sum_{n=1}^2 \left(\Delta_n - i \frac{\gamma_n^s}{2} \right) \sigma_n^+ \sigma_n^-, \quad (1)$$

where $J_{mn} = \frac{1}{2} \sqrt{\beta_m \beta_n \Gamma_m \Gamma_n} \sin \phi_{mn}$ and $\Gamma_{mn} = \sqrt{\beta_m \beta_n \Gamma_m \Gamma_n} \cos \phi_{mn}$ are the dispersive and dissipative coupling rates connecting QD_m and QD_n. $\Gamma_m = \gamma_m^{wg} + \gamma_m^s$ contains the decay rate into (out of) the waveguide γ_m^{wg} (γ_m^s), corresponding to β -factors $\beta_m = \gamma_m^{wg}/\Gamma_m$. Δ_m is the detuning of QD_m with respect to the excitation field frequency, such that $\Delta_{mn} = \Delta_m - \Delta_n$ is the detuning between the two QDs, $\phi_{mn} = k|z_{mn}|$ is the phase lag due to the emitter separation z_{mn} with k being the effective wavenumber of the PCW mode. ϕ_{mn} determines the character of the coupling between dispersive

* These authors contributed equally to this work.

† Email to: alexey.tiranov@nbi.ku.dk; lodahl@nbi.ku.dk

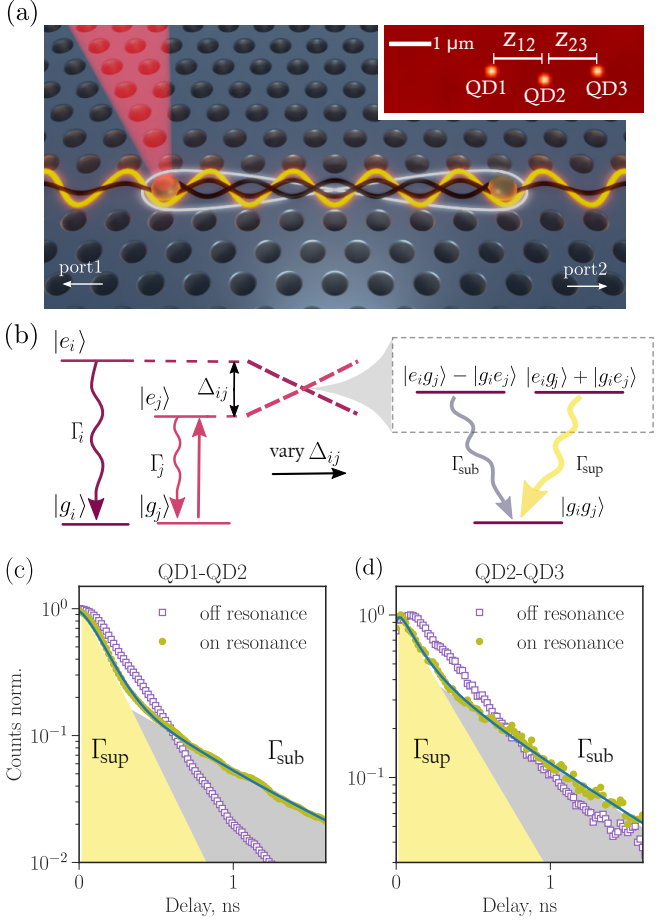


FIG. 1. (color online) **Observation of the super- and subradiant emission.** (a) Illustration of the photon-mediated coupling between two QDs in a PCW where one QD is optically pumped. Subsequently, the emission dynamics of the coupled QD system exhibits super- and subradiance originating from either constructive (bright line) or destructive (dark line) interference of the field emitted to the PCW and scattered by each of the QDs. The inset shows a fluorescence image of the QDs in the PCW where $z_{12} = 1.25(3)$ μm , $z_{23} = 0.96(3)$ μm . (b) Energy level diagram of two QDs with a mutual detuning of Δ_{mn} . Off resonance (left image) the two QDs decay independent of each other while on resonance (right image) super- and subradiant dynamics occurs with rates Γ_{sup} and Γ_{sub} , respectively. (c) and (d) Measured time-resolved emission dynamics of pair QD1-QD2 and QD2-QD3 both on and off resonance and after exciting QD2 and QD3 through a higher energy excited states. The measured count rates are normalised to the maximum at zero time delay corresponding to the time of excitation of the coupled system. The solid lines are the model fits to the experimental data. Off resonance, $\Delta_{12}/2\pi = 6$ GHz, ($\Delta_{23}/2\pi = 5$ GHz) the decay curve corresponds to the cases of individual QDs. When two QDs are brought into resonance, two decay components are observed in the data, a fast Γ_{sup} and a slow Γ_{sub} corresponding to super- and subradiant dynamics.

($\Gamma_{mn} = 0$), which modifies the energy levels, to dissipative

($J_{mn} = 0$), which affects the decay dynamics. The system bears resemblance to the case of a nanocavity where each QD acts as an end mirror by scattering single photons into the mode of the waveguide and ϕ_{mn} determines the cavity resonance condition, see FIG. 1a. Notably the system is of inherently quantum character since the QDs can only scatter a single photon at a time. σ_m^+, σ_n^- are the raising and lowering operators for the optical transition of QD_{*m*}, QD_{*n*}. By selectively pumping one of the QDs, e.g QD_{*n*}, one excitation is launched to populate the state $|g_m e_n\rangle$. On resonance ($\Delta_{mn} = 0$), the subsequent dynamics is best described in terms of the entangled eigenstates $|S\rangle = (|e_m g_n\rangle + |g_m e_n\rangle)/\sqrt{2}$ and $|s\rangle = (|e_m g_n\rangle - |g_m e_n\rangle)/\sqrt{2}$ with the associated decay rates determined by the phase lag ϕ_{mn} . $\phi_{mn} = N\pi$ (*N* integer) corresponds to dissipative coupling between QDs leading to a superradiant $|S\rangle$ and a subradiant $|s\rangle$ state with modified decay rates, see FIG. 1b). $\phi_{mn} = (N + 1/2)\pi$ corresponds to dispersive coupling where the collective states are shifted by J_{mn} , while leaving their decay rates unchanged compared to the uncoupled emitters. In the present experiment, we are primarily studying the regime of dissipative radiative coupling leading to modified emission dynamics.

To observe collective dynamics experimentally, we optically excite a single QD and record the collective emission dynamics from either collection port 1 or 2 studying three different QDs (QD1-3, see inset of FIG. 1a). Two examples of recorded emission are shown in FIG. 1c,d where we alter the detuning to compare the off- and on-resonance cases, see Supplemental Notes for further experimental details. On resonance, we observe strongly modified decay dynamics due to coherent coupling, and both super- and subradiant features are directly visible. For QD1-QD2, we find radiative linewidths of $\Gamma_{\text{sup}}/2\pi = 1.36(8)$ GHz and $\Gamma_{\text{sub}}/2\pi = 0.280(2)$ GHz, by modelling the data with a bi-exponential decay. These values should be referred to the single emitter linewidths of $\Gamma_2/2\pi = 0.79(2)$ GHz and $\Gamma_1/2\pi = 0.85(1)$ GHz, respectively, as observed far off-resonance where the coupling is negligible. We derive a super/subradiant enhancement factor of 4.8. The enhancement factor is a direct figure-of-merit of the quality of the collective coupling, and is highly sensitive to experimental imperfections and decoherence; for a detailed account of the underlying physical parameters, see Supplemental Notes Table II. The long-range nature of the dipole-dipole coupling is explicitly demonstrated. Using resonant excitation through the PCW, we image the spatial separation of the QDs and find $z_{12} = 1.25(3)$ μm and $z_{23} = 0.96(3)$ μm (see inset of FIG. 1a), which should be compared to the wavelength $\lambda = 270$ nm inside GaAs or the PCW lattice constant of $a = 240$ nm.

Next, we show coherent evolution of collective states by precisely controlling the detuning between two emitters. We start by resonantly exciting a single QD to prepare $|eg\rangle = (|S\rangle + |s\rangle)/\sqrt{2}$, i.e. an equal superposition of the super- and subradiant states. The state

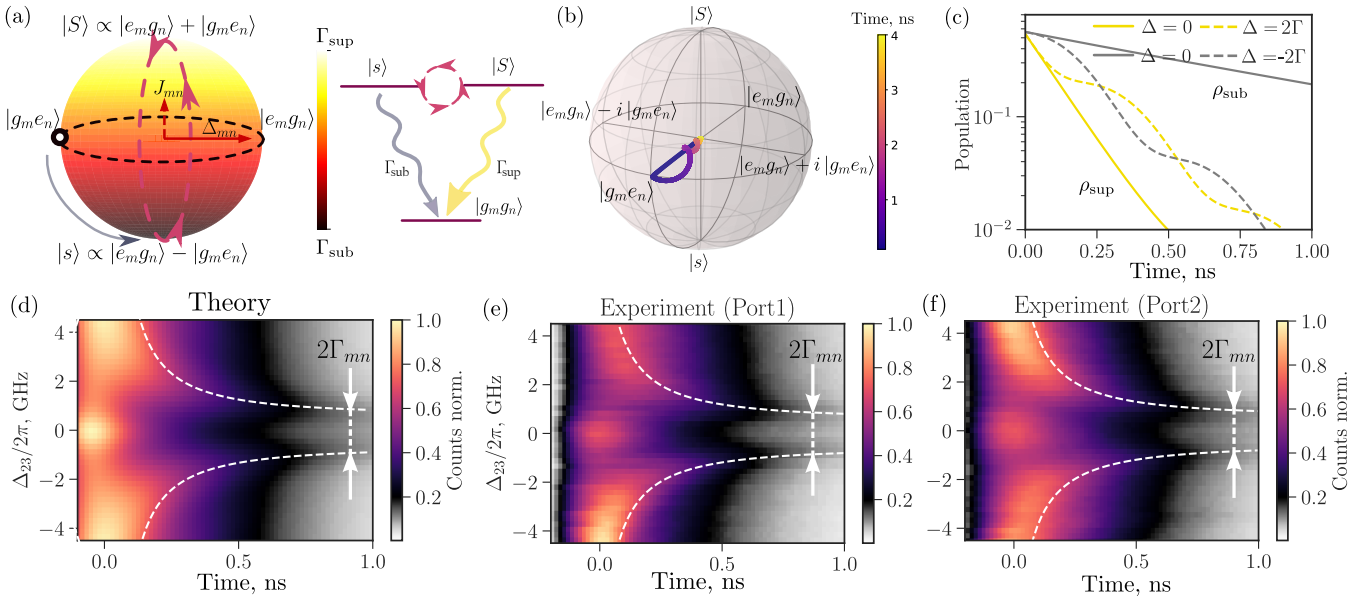


FIG. 2. (color online) **Coherent dynamics of coupled QDs.** (a) The evolution of a single collective excitation can be represented on a Bloch sphere with the color indicating the decay rate of the respective collective state. After exciting QD_n, the state $|g_m e_n\rangle$ is populated. Two processes occur: exponential decay by spontaneous emission (black solid arrow) and coherent evolution between super- and subradiant states (red arrow) as determined by the detuning between the two QDs Δ_{mn} . (b) Exemplary state evolution trajectory for $\Delta = -5.5\Gamma$, where the length of the Bloch vector shows the population in the single-excitation subspace. The color bar tracks the evolution time from preparing the coupled system in the initial state and until decaying to the ground state $|g_m g_n\rangle$ (origin of Bloch sphere). (c) Calculated population of the collective states as a function of time for two values of detuning and comparing super- (yellow curves) and subradiant (grey curves) contributions for an initial state $|g_m e_n\rangle$. The corresponding emission intensity is plotted in (d). The calculation is done with the experimentally extracted parameters of the QD2-QD3 pair (see Supplemental Notes). (e) Full experimental dataset for a continuous scan of detuning Δ_{23} and comparing measurements from outcoupling port 1 (e) and port 2 (f). The dashed lines trace the maximum population after the first oscillation and is given by $t = \pi/f_{\text{osc}}$, see main text for the definitions.

subsequently evolves in time into a collective state, see the Bloch sphere graphical representation in FIG. 2a. The color of the Bloch sphere surface represents the decay time of the respective state, and the collective state vector precesses due to coherent evolution. Assuming $\Gamma_m = \Gamma_n$, the correlated dynamics is described by the difference between the two eigenvalues of the coupled system $f_{\text{osc}} = \sqrt{\Delta_{mn}^2 + (2J_{mn} - i\Gamma_{mn})^2}$. For, e.g., the case of pure dissipative coupling ($J_{mn} = 0$) two different regimes are identified, cf. FIG. 2c,d. In the underdamped regime, $|\Delta_{mn}| > \Gamma_{mn}$, coherent evolution prevails over dissipation resulting in the observation of an increase in emission intensity. The dashed lines in FIG. 2d-f track the observed intensity maximum for different values of Δ_{mn} . In the overdamped regime, $|\Delta_{mn}| < \Gamma_{mn}$, the dissipative coupling damps the excitation to the ground state faster than the coherent oscillations on the Bloch sphere (leading to the “gap” between two dashed lines on FIG. 2d). $\Delta_{mn} = \Gamma_{mn}$ is the case of critical damping where the dissipation and coherent oscillation rates are balanced. These examples quantify how precise emitter tuning provides an experimentally accessible “control knob” of coupled collective quantum states.

The observed rich coherent dynamics of the

collectively-coupled system is evident from the experimental data displayed in FIG. 2e,f that are very well reproduced by theory. As discussed above for the resonant case, following a fast decay of the superradiant component, the coupled system evolves towards the subradiant state. In the detuned case, coherent evolution is observed leading to modified dynamics since super- and subradiant components are interchanged. The oscillation between super- and subradiant components, as defined by the detuning, leads to an increase of the intensity corresponding to the superradiant component being maximal. This is clearly visible as a bright region, as is tracked by the dashed line on FIG. 2d-f. By comparing the emission from two different directions (outcoupling port 1 and 2), we observe a very similar behavior (cf. FIG. 2e,f), which is consistent with a predominantly dissipative coupling $\phi_{mn} \simeq N\pi$. The experiment was repeated on in total three pairs of QDs, where the additional data and detailed modelling can be found in the Supplemental Notes. For all three data sets we observe predominantly dissipative coupling, which likely results from the fact that QD candidates featuring efficient coupling to the PCW were pre-selected in the experiment based on resonant transmission measurements through the waveguide (see Supplemental Notes).

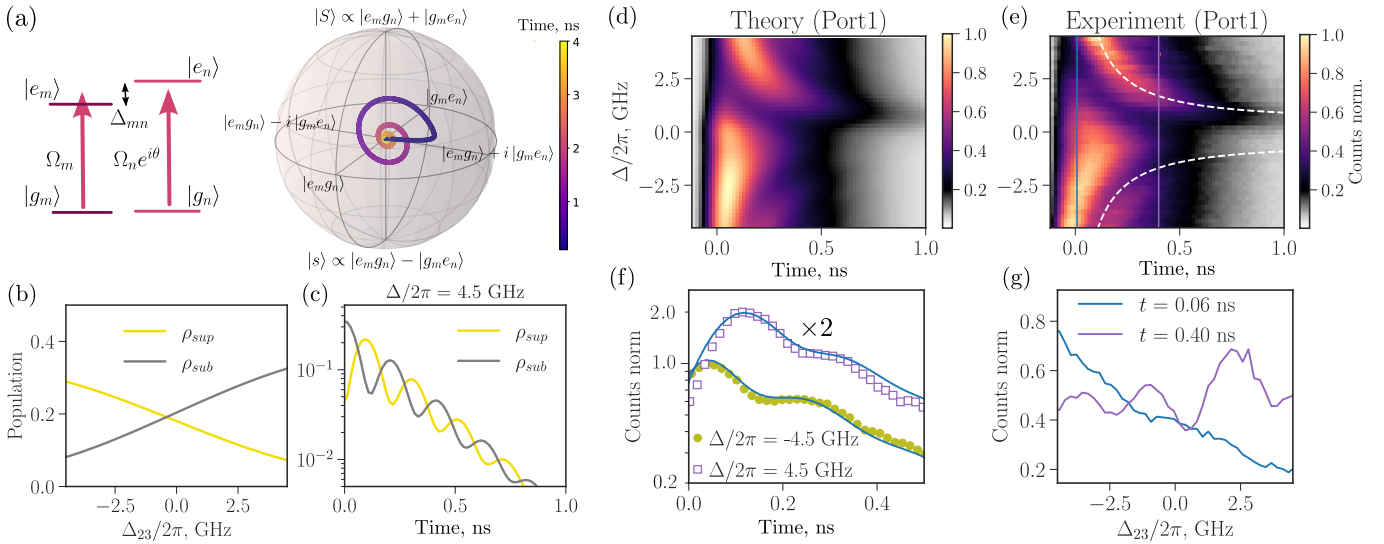


FIG. 3. (color online) **Controlled preparation of the collective state.** (a) Simultaneous driving of both QDs with control of the phase θ allows to initialise the system in a collective state. In the case of $\theta \approx -\pi/2$ the initial state in the single-excitation subspace is close to $|ge\rangle + i|eg\rangle$. The detuning between the QDs results in evolution of the collective state towards $|S\rangle$ when $\Delta < 0$ and towards $|s\rangle$ for $\Delta > 0$. An example of the state trajectory for $\Delta < 0$ is depicted on the Bloch sphere. (b) The population of the super- ρ_{sup} and subradiant ρ_{sub} components during the excitation as a function of the detuning Δ for $\theta \approx -\pi/2$. The sign of the detuning determines whether the super- or subradiant states are preferentially populated. (c) The two populations are oscillating out of phase as a function of time after excitation. (d) Calculated and (e) measured intensity decay dynamics as a function of detuning and collected from the outcoupling port 1. The asymmetric dependence on detuning is very well reproduced by the theory using parameters extracted from the experiment with $\theta \approx -\pi/2$. (f) Examples of emission intensity decay curves for two values of detuning explicitly displaying the coherent oscillations being out-of-phase of each other as determined by the sign of the detuning. (g) Normalised counts as a function of detuning and for two representative times quantifying the asymmetry.

This condition results in selection of QDs close to the waveguide center and therefore a phase lag between QDs primarily determined by the periodicity of the photonic crystal lattice. Since the PCW coupling is large close to the band edge of the waveguide mode, this leads to $k/a \simeq \pi$ [14], whereby the phase lag between neighbouring PCW unit cells is $\simeq \pi$, see Supplemental Notes for further details.

The theoretical model (FIG. 2d) reproduces the experimental data and fully captures the complex coherent quantum dynamics observed experimentally (see FIG. 2e,f). From the analysis, we extract for pair QD2-QD3: $\Gamma_{23}/2\pi = 0.61$ GHz and $J_{23}/2\pi = 0.03$ GHz. The dissipative coupling rate is comparable to the intrinsic linewidth of the respective QDs, while the dispersive part is almost vanishing. As opposed to the case of superconducting qubits [9], changing the detuning between the QDs has a negligible effect on the phase-lag whereby the coupling remains dissipative. This is a consequence of the fact that the detuning is vanishingly small compared to the optical frequency. This distinction may be advantageous in applications of radiative collective coupling, since it allows the detuning to be exploited as a control parameter without changing the coupling, which is explicitly demonstrated in the present work. Interestingly, even when the emitter-emitter system is initialised in $|eg\rangle$ or $|ge\rangle$, coherent oscillations are still observed. This is en-

abled by the fast decay of the superradiant component after initialisation leading to the population of the slower decaying subradiant state that coherently evolves on the Bloch sphere (see FIG. 2b).

The deterministic preparation of collective states is essential in order to pave the way for their applications in quantum-information processing. To this end, we coherently excite both QDs in order to control the initial collective state on the Bloch sphere, see FIG. 3a. In the magnetic Zeeman field, the coupled QD transitions are orthogonally (circularly) polarized [30], yet they are efficiently coupled by the optical mode of the PCW. The phase between the two driving fields Ω_2 and $\Omega_3 e^{i\theta}$ is adjusted via the polarization of the excitation laser and by using a single laser we implement $\theta \approx -\pi/2$, which prepares an initial state close to $|eg\rangle + i|ge\rangle$ for $\Delta = 0$. With detuning, the state either evolves towards the super- (for $\Delta > 0$) or the subradiant (for $\Delta < 0$) state. This results in a striking difference in the radiation at short time followed by out-of-phase coherent oscillations between the two components, see FIG. 3b,c.

The experimental demonstration of this behavior is shown in FIG. 3e, which is very well described by the theory shown in FIG. 3d. We observe a pronounced asymmetry around zero detuning, where for positive detunings the emission dynamics is effectively delayed. This stems from the selective population of the subradiant state re-

sulting in lower emission at early times. Subsequently the emission intensity increases as the coherent evolution increases the population of the superradiant state. The reverse behavior is found for $\Delta < 0$. This is a result of the out-of-phase oscillation of the population of the super- and subradiant components, see FIG. 3f,g. As opposed to the case where a single QD was excited, cf. data FIG. 2, we observe here multiple coherent oscillations. This is explained by that the prepared state $|eg\rangle + i|ge\rangle$ starts to coherently evolve on the Bloch sphere directly after the excitation, in contrast to preparing $|eg\rangle$ for which the coherent evolution becomes effective only as the state decays to $|s\rangle$. We track the maximum emission intensity (dashed line) for $\Delta > 0$ (and minimum for $\Delta < 0$) in the plots of FIG. 3d,e. It is consequently found that the collective light emission intensity can be controlled via the QD detuning.

In conclusion, we have observed super- and subradiant emission dynamics using pairs of QDs embedded in PCWs and separated by a distance much larger than the wavelength. This is facilitated by the PCW offering broadband spectral operation and long-range photon-mediated coherent interaction between QDs. We also demonstrated how to manipulate the superradiant and subradiant state dynamics by controlling the detuning and pumping conditions. The deterministic nature of the photon-emitter coupling will lead to a whole new range of opportunities when implementing a coherent spin inside the QD [30, 31]. For instance, advanced photonic cluster

states may be generated deterministically [32] providing a universal resource for measurement-based photonic quantum computing. To this end, waveguide-mediated dissipative coupling can be exploited to realize spin-spin entanglement between distant quantum emitters [33]. Another direction will exploit photon scattering from coupled QDs to realize efficient Bell-state measurements [34] or photon-photon quantum gates [35]. In a broader perspective, the ability to deterministically couple multiple quantum emitters opens a new arena of studying non-equilibrium quantum many-body physics of strongly correlated light and matter of possible use in quantum simulations of strongly correlated condensed matter systems [12].

ACKNOWLEDGMENTS

The authors thank Xiao-Liu Chu for fruitful discussions at the beginning of the project. We gratefully acknowledge financial support from Danmarks Grundforskningsfond (DNRF 139, Hy-Q Center for Hybrid Quantum Networks). BS acknowledges financial support from Deutsche Forschungsgemeinschaft (DFG, German Research Foundation), Grant No. 449674892. OS acknowledges funding from the European Union's Horizon 2020 research and innovation programme under the Marie Skłodowska-Curie grant agreement No. 801199.

[1] J. L. O'Brien, A. Furusawa, and J. Vučković, *Nature Photonics* **3**, 687 (2009).

[2] R. Uppu, L. Midolo, X. Zhou, J. Carolan, and P. Lodahl, *Nature Nanotechnology* **16**, 1308 (2021).

[3] E. M. Purcell, *Phys. Rev.* **69**, 674 (1946).

[4] R. H. Dicke, *Phys. Rev.* **93**, 99 (1954).

[5] M. O. Scully, *Phys. Rev. Lett.* **115**, 243602 (2015).

[6] P. W. Anderson, *Science* **177**, 393 (1972).

[7] R. G. DeVoe and R. G. Brewer, *Phys. Rev. Lett.* **76**, 2049 (1996).

[8] J. Eschner, C. Raab, F. Schmidt-Kaler, and R. Blatt, *Nature* **413**, 495 (2001).

[9] A. F. van Loo, A. Fedorov, K. Lalumière, B. C. Sanders, A. Blais, and A. Wallraff, *Science* **342**, 1494 (2013).

[10] J.-B. Trebbia, Q. Deplano, P. Tamarat, and B. Lounis, *Nature Communications* **13**, 2962 (2022).

[11] R. E. Evans, M. K. Bhaskar, D. D. Sukachev, C. T. Nguyen, A. Sipahigil, M. J. Burek, B. Machielse, G. H. Zhang, A. S. Zibrov, E. Bielejec, H. Park, M. Lončar, and M. D. Lukin, *Science* **362**, 662 (2018).

[12] C. Noh and D. G. Angelakis, *Reports on Progress in Physics* **80**, 016401 (2016).

[13] D. E. Chang, J. S. Douglas, A. González-Tudela, C.-L. Hung, and H. J. Kimble, *Rev. Mod. Phys.* **90**, 031002 (2018).

[14] P. Lodahl, S. Mahmoodian, and S. Stobbe, *Rev. Mod. Phys.* **87**, 347 (2015).

[15] A. S. Sheremet, M. I. Petrov, I. V. Iorsh, A. V. Poshakinskiy, and A. N. Poddubny, *arXiv* **2103.06824** (2021).

[16] V. E. Elfving, S. Das, and A. S. Sørensen, *Phys. Rev. A* **100**, 053843 (2019).

[17] A. Asenjo-Garcia, M. Moreno-Cardoner, A. Albrecht, H. J. Kimble, and D. E. Chang, *Phys. Rev. X* **7**, 031024 (2017).

[18] J. D. Brehm, A. N. Poddubny, A. Stehli, T. Wolz, H. Rotzinger, and A. V. Ustinov, *npj Quantum Materials* **6**, 10 (2021).

[19] E. Kim, X. Zhang, V. S. Ferreira, J. Bunker, J. K. Iverson, A. Sipahigil, M. Bello, A. González-Tudela, M. Mirhosseini, and O. Painter, *Phys. Rev. X* **11**, 011015 (2021).

[20] M. Zanner, T. Orell, C. M. F. Schneider, R. Albert, S. Oleschko, M. L. Juan, M. Silveri, and G. Kirchmair, *Nature Physics* **18**, 538 (2022).

[21] H. J. Kimble, *Nature* **453**, 1023 (2008).

[22] M. Gross and S. Haroche, *Physics Reports* **93**, 301 (1982).

[23] X.-L. Chu, V. Angelopoulou, P. Lodahl, and N. Rotenberg, *arXiv* **2206.00573** (2022).

[24] J.-H. Kim, S. Aghaeimeibodi, C. J. K. Richardson, R. P. Leavitt, and E. Waks, *Nano Letters* **18**, 4734 (2018).

[25] J. Q. Grim, A. S. Bracker, M. Zalalutdinov, S. G. Carter, A. C. Kozen, M. Kim, C. S. Kim, J. T. Mlack, M. Yakes, B. Lee, and D. Gammon, *Nature Materials* **18**, 963 (2019).

- [26] Z. X. Koong, M. Cygorek, E. Scerri, T. S. Santana, S. I. Park, J. D. Song, E. M. Gauger, and B. D. Gerardot, *Science Advances* **8**, eabm8171 (2022).
- [27] J. Q. Grim, I. Welland, S. G. Carter, A. S. Bracker, A. Yeats, C. S. Kim, M. Kim, K. Tran, I. Vurgaftman, and T. L. Reinecke, *Phys. Rev. B* **106**, L081403 (2022).
- [28] C. Hettich, C. Schmitt, J. Zitzmann, S. Kühn, I. Gerhardt, and V. Sandoghdar, *Science* **298**, 385 (2002).
- [29] A. Albrecht, L. Henriet, A. Asenjo-Garcia, P. B. Dieterle, O. Painter, and D. E. Chang, *New Journal of Physics* **21**, 025003 (2019).
- [30] R. J. Warburton, *Nature Materials* **12**, 483 (2013).
- [31] M. H. Appel, A. Tiranov, S. Pabst, M. L. Chan, C. Starup, Y. Wang, L. Midolo, K. Tiurev, S. Scholz, A. D. Wieck, A. Ludwig, A. S. Sørensen, and P. Lodahl, *Phys. Rev. Lett.* **128**, 233602 (2022).
- [32] S. E. Economou, N. Lindner, and T. Rudolph, *Phys. Rev. Lett.* **105**, 093601 (2010).
- [33] M. Gullans, T. G. Tiecke, D. E. Chang, J. Feist, J. D. Thompson, J. I. Cirac, P. Zoller, and M. D. Lukin, *Physical Review Letters* **109** (2012), 10.1103/PhysRevLett.109.235309.
- [34] J. Borregaard, A. S. Sørensen, and P. Lodahl, *Advanced Quantum Technologies* **2**, 1800091 (2019).
- [35] B. Schrinski and A. S. Sørensen, *arXiv* **2110.15878** (2021)

Supplementary Notes - Coherent super- and subradiant dynamics between distant optical quantum emitters

Alexey Tiranov^{†, 1,*} Vasiliki Angelopoulou,^{1,*} Cornelis Jacobus van Diepen,¹ Björn Schrinski,¹ Oliver August Dall’Alba Sandberg,¹ Ying Wang,¹ Leonardo Midolo,¹ Sven Scholz,² Andreas Dirk Wieck,² Arne Ludwig,² Anders Søndberg Sørensen,¹ and Peter Lodahl^{1, †}

¹Center for Hybrid Quantum Networks (Hy-Q), The Niels Bohr Institute, University of Copenhagen, DK-2100 Copenhagen Ø, Denmark

²Lehrstuhl für Angewandte Festkörperphysik, Ruhr-Universität Bochum, Universitätsstraße 150, D-44801 Bochum, Germany

(Dated: October 6, 2022)

CONTENTS

Acknowledgments	5
I. Theoretical model	1
II. Sample and optical setup	5
III. Optical spectroscopy	6
IV. QD imaging	9
V. ‘Off-resonant’ excitation	9
VI. Resonant excitation	15
References	19

I. THEORETICAL MODEL

The theoretical description is based on the master equation for the system, which reads ($\hbar = 1$)

$$\dot{\rho} = \mathcal{L}_{\text{tot}}[\rho] = -i[H, \rho] + \mathcal{L}_{\text{coup}}[\rho] + \mathcal{L}_{\text{decay}}[\rho] + \mathcal{L}_{\text{deph}}[\rho]. \quad (\text{S1})$$

Here the Hamiltonian $H = \sum_m \Delta_m \sigma_m^z / 2 + \Omega_m (e^{i\theta_m} \sigma_m^+ + e^{-i\theta_m} \sigma_m^-) / 2$ accounts for the detuning and potential driving of the involved emitters with relative phases $\theta_m - \theta_n$. In our treatment we include three different Liouvillians. The first one $\mathcal{L}_{\text{coup}}[\rho]$ describes the waveguide mediated coupling. This term is the main focus of this work and is discussed in detail below. Additionally, we include a Liouvillian corresponding to decay of the emitters to modes other than the waveguide (side modes)

$$\mathcal{L}_{\text{decay}}[\rho] = \sum_m \gamma_m^s \sigma_m^- \rho \sigma_m^+ \quad (\text{S2})$$

with a decay rate γ_m^s for the m th emitter. Finally we also include dephasing described by

$$\mathcal{L}_{\text{deph}}[\rho] = \frac{\gamma_d}{2} \sum_m [\sigma_m^z \rho \sigma_m^z - \rho], \quad (\text{S3})$$

where the dephasing rate γ_d is assumed similar for both emitters for simplicity. This is the standard description of pure dephasing acting individually on each emitter.

* These authors contributed equally to this work.

† Email to: alexey.tiranov@nbi.ku.dk; lodahl@nbi.ku.dk

To describe the waveguide mediated coupling we use the well known rotating-wave approximated Jaynes-Cummings coupling Hamiltonian in one dimension $H' = \sum_m \int dk (g_{k,m} \sigma_m^+ a_k + g_{k,m}^* a_k^\dagger \sigma_m^-)$ with light mode creation operators a^\dagger and Pauli operators $\sigma_m^\pm = |e\rangle_m \langle g|_m$ for different QD sites labelled with $m = 1, 2, 3$. The coupling of the light modes to the dipoles is given by $g_{k,m} \sim \mathbf{E}_k(\mathbf{r}_m) \cdot \mathbf{d}_m$, i.e., the electrical field mode solution in the waveguide at coordinate \mathbf{r}_m times the dipole vector of the m th QD.

The experiment is conducted in mirror-symmetric PCWs that have primarily linear local polarization, so that effects of directional chiral light-matter coupling can be ignored [S1], i.e. coupling coefficients for left and right propagation are of equal magnitude: $|g_{k,m}| \approx |g_{-k,m}|$. The absence of chirality assumed here is experimentally confirmed by comparing amplitudes of resonant transmission dips FIG. S7 while sweeping the external magnetic field in two opposite directions. For this we look at the amplitude ratios between two dipoles for each QD as a function of external magnetic field (FIG. S8). We repeated the same measurement with the direction of the magnetic field reversed (FIG. S8). The results show ‘mirror’ symmetry around zero magnetic field up to 4 T, confirming the assumption of non-chiral interaction.

According to Bloch’s theorem we can write the electric field in the periodic waveguide as $\mathbf{E}_k(\mathbf{r}) = \mathbf{U}_k(\mathbf{r})e^{ikz}$ with a periodic $\mathbf{U}_k(\mathbf{r})$. As we argue in Sec. V below, the procedure used to select QDs favors dots located at the same position within the unit cell so that $\mathbf{U}_k(\mathbf{r}_m)$ is similar for all QDs. In combination with the linear polarization, this means that apart from an overall phase, which can be absorbed by changing the origin of the z -axis, we can chose the mode function to be real $\mathbf{U}_k(\mathbf{r}_m) \in \mathbb{R}^3$ for all QDs. Due to time reversal symmetry of the waveguide solutions $\mathbf{E}_k = \mathbf{E}_{-k}^*$ we also have real mode function in the backward direction since $\mathbf{U}_{-k} = \mathbf{U}_k$. Furthermore, apart from the propagation phases (e^{ikz}), the fact that $\mathbf{U}_k(\mathbf{r}_m)$ is real means that any phase of the coupling constant can only arise from the dipole moment of the transition. Since this dipole moment is the same for the coupling to all modes, any phase in the dipole moment can be absorbed by a redefinition of σ_m^- . We thus choose real coupling constants in the following and the phases that appear will be due to propagation. It is noted that any net phases due to the QDs not having the same position within the unit cell can be incorporated into the definition of the phase ϕ_{mn} below, but the assumption of real coupling constants simplify the description.

Integrating out the photonic degrees of freedom in the Markov approximation leads to the Liouvillian for the waveguide mediated coupling [S2–S4]

$$\mathcal{L}_{\text{coup}}[\rho] = i \sum_{mn} J_{mn} [\sigma_n^+ \sigma_m^-, \rho] - \sum_{mn} \Gamma_{mn} \left[\sigma_m^- \rho \sigma_n^+ - \frac{1}{2} \{ \sigma_n^+ \sigma_m^-, \rho \} \right] \quad (\text{S4})$$

with the couplings

$$\Gamma_{mn} = \frac{4\pi |g_{k_0,m}| |g_{k_0,n}|}{c} \text{Re}\{e^{i\phi_{mn}}\} \quad \text{and} \quad J_{mn} = \frac{2\pi |g_{k_0,m}| |g_{k_0,n}|}{c} \text{Im}\{e^{i\phi_{mn}}\}, \quad (\text{S5})$$

which corresponds to the expressions in the main text with the identification $\Gamma_m \beta_m = 4\pi |g_{k_0,m}|^2 / c$. Here the coupling depends on quantities evaluated at the resonant wavenumber k_0 . To ease the notation we omit the subscript and simply denote it k in the main text and below. The nature of the interaction between the emitters depends crucially on the propagation phase $\phi_{mn} = k|z_{mn}|$ with $|z_{mn}|$ being the distance between emitters m and n . This phase describes the interference of excitations switching back and forth between the emitters and determine whether the interaction is dispersive $|\Gamma_{mn}| \ll |J_{mn}|$ for $\phi_{mn} \approx (N + 1/2)\pi$ or dissipative $|J_{mn}| \ll |\Gamma_{mn}|$ for $\phi_{mn} \approx N\pi$ with N being an integer.

In addition to the master equation for the QDs we also need to relate the density matrix to the outgoing fields. These can be determined by the well-known input-output formalism [S5]. In case of excitation from the side, i.e., not through the waveguide, the left- and right-going fields are given by (assuming the three QDs are labeled in ascending order from left to right)

$$E_L = \sum_n e^{i\phi_{1n}} E_n \quad \text{and} \quad E_R = \sum_n e^{i\phi_{n3}} E_n, \quad (\text{S6})$$

where $E_n = -i \frac{\sqrt{\beta_n \Gamma_n} \sigma_n^-}{\sqrt{2}}$. The intensities are given by the squared modulus of the fields $I_{L/R} = |E_{L/R}|^2$.

The theoretical results depicted throughout the main text are obtained via numerical integration of Eq. (S1). To account for spectral diffusion we average all results over a normal distribution of detunings Δ_m with standard deviation σ_{sd} . Alternatively, for a simplified analytical treatment, we can ignore dephasing and only consider the dynamics in the single excitation subspace. In this case the master equation (S1) reduces to

$$\dot{\rho} = -i \left[\mathcal{H}_{\text{eff}} \rho - \rho \mathcal{H}_{\text{eff}}^\dagger \right] \quad (\text{S7})$$

with the effective Hamiltonian given in Eq. (1) of the main text.

To understand the properties of the emitted light we now turn to general symmetry properties that arise for pure dissipative coupling, i.e. $\phi_{mn} = N\pi$; the experimental scenario observed here. Writing the emitted field from the m th QD as an arbitrary field $E_m = |E_m|e^{i\phi_m}$ (i.e., only restricted to emit the same field in both directions) the intensities can be expressed as

$$I_L = \sum_{mn} |E_m||E_n| \cos(\phi_{mn} - \phi_m + \phi_n), \quad (S8)$$

$$I_R = \sum_{mn} |E_m||E_n| \cos(\phi_{mn} + \phi_m - \phi_n). \quad (S9)$$

For purely dissipative coupling we thus have $I_L = I_R$ since the cosine is an even function around $\phi_{mn} = N\pi$, making the signal equal at both detectors for *arbitrary* phases ϕ_m . The symmetry ($\Delta_{mn} \rightarrow -\Delta_{mn}$) in detuning $\Delta_{mn} = \Delta_m - \Delta_n$ between the different QDs can be explained by observing that in case of purely dissipative coupling, the only imaginary contribution to the master equation (S1), apart from potential phases in the driving, arises from terms $\propto \Delta_m \sigma_m^z$. Thus, changing $\Delta_m \rightarrow -\Delta_m$ leads to complex conjugation of the Liouvillian $\mathcal{L}_{\text{tot}} \rightarrow \mathcal{L}_{\text{tot}}^*$ and we have $e^{\mathcal{L}_{\text{tot}}^* t}[\rho^*] = (e^{\mathcal{L}_{\text{tot}} t}[\rho])^*$, i.e. the master equation is solved by the complex conjugated density matrix ρ^* . Since $\rho(t) \rightarrow \rho^*(t)$ does not affect measurement results if Eq. (S6) is real ($\phi_{mn} = N\pi$), it follows that for initially real $\rho = \rho^*$, e.g. for a single QD quickly excited to the excited state, the time evolution will produce the same intensity for opposite detunings. On the other hand, driving two QDs simultaneously can induce a complex phase between the QDs that breaks the symmetry, as is experimentally observed and discussed in the main text.

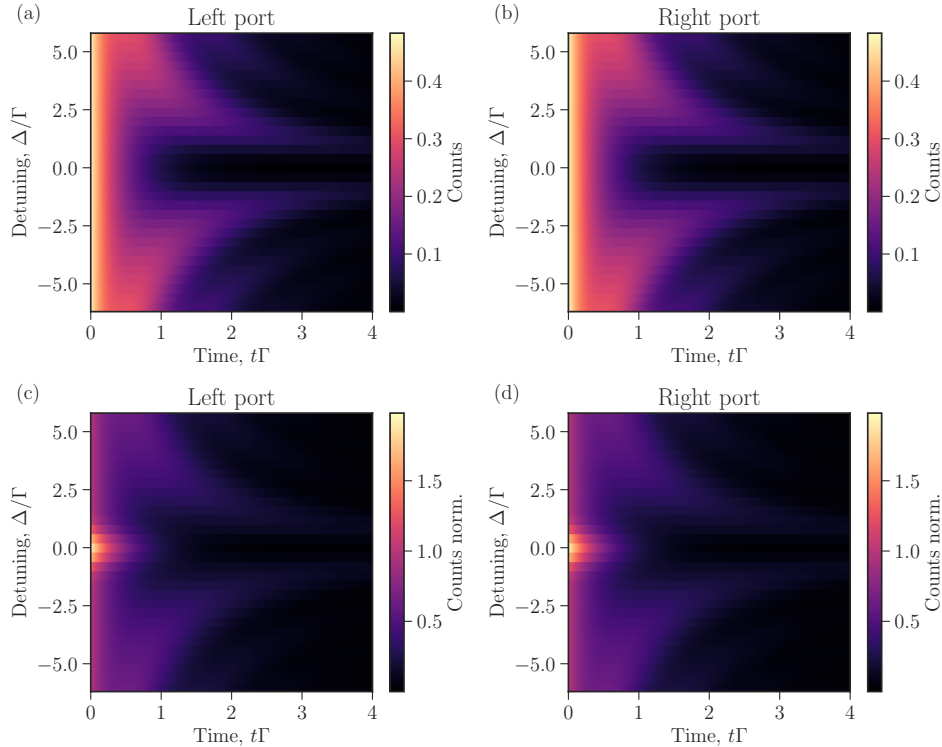


FIG. S1. Exemplary calculated time resolved intensities for left (a,c) and right (b,d) ports according to the analytical results Eq. (S10), in qualitative agreement with the experimental data from the main text. The normalisation to the sum of each time trace was used for (b,d). The following parameters are assumed: $\phi_{12} = 0$, $\beta_1 = \beta_2 = 0.99$, $\Gamma_1 = \Gamma_2 = \Gamma$, $\gamma_d = 0$.

To be able to give analytical expressions for the output fields of two QD close to resonance we assume the initial π -flip (exciting the left QD) to be quasi instantaneous compared to the lifetimes $1/\Gamma_1, 1/\Gamma_2$ and neglect dephasing ($\gamma_d = 0$). For this simplified scenario we can give concise output fields arriving at the right detector at time t

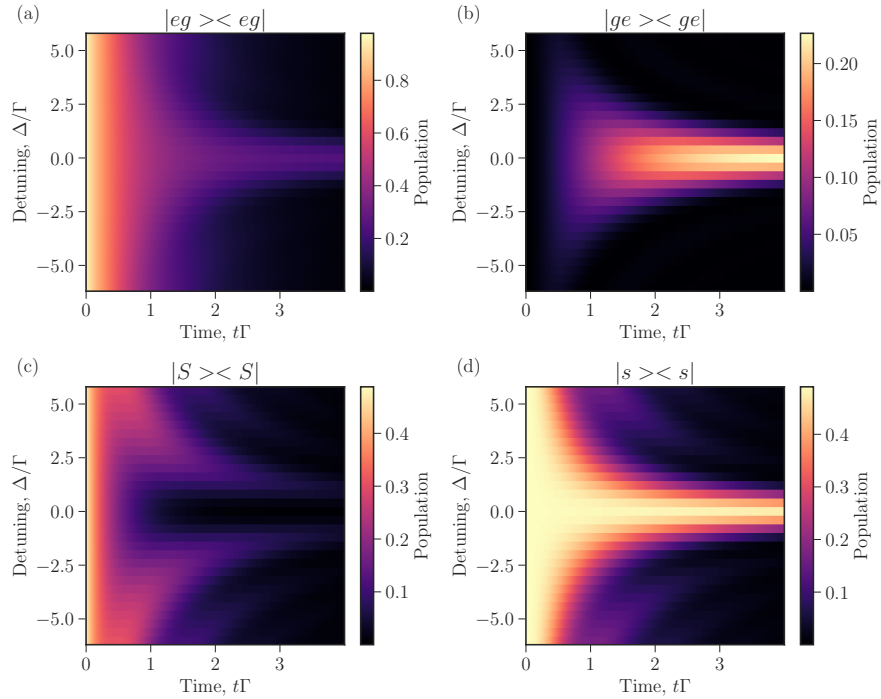


FIG. S2. Theoretical population of the different density matrix entries (which are not directly accessible in the experiment): Due to the decay of the superradiant state $|S\rangle$, the excitation $|eg\rangle\langle eg|$ gets redistributed to the other QD $|ge\rangle\langle ge|$ in the shape of the subradiant state $|s\rangle$, which exhibits an extremely long lifetime if close to $\Delta = 0$. For larger detunings we observe oscillations between $|S\rangle$ and $|s\rangle$ that quickly die out due to the fast emission of the superradiant state. Same parameters as for FIG. S1 were used.

$E^R(t) = E_{\text{sup}}^R(t) + E_{\text{sub}}^R(t)$ with the (original) super- and subradiant contributions

$$\begin{aligned} E_{\text{sup}}^R(t) &= \frac{-i\sqrt{\Gamma_1\beta_1}(\Gamma_2\beta_2 - i\Delta + (S + \Gamma_1 - \Gamma_2)/2)}{\sqrt{2}S} \exp\left[-(\Gamma_1 + \Gamma_2 + S)\frac{t}{4}\right] \\ E_{\text{sub}}^R(t) &= \frac{i\sqrt{\Gamma_1\beta_1}(\Gamma_2\beta_2 - i\Delta + (-S + \Gamma_1 - \Gamma_2)/2)}{\sqrt{2}S} \exp\left[-(\Gamma_1 + \Gamma_2 - S)\frac{t}{4}\right], \end{aligned} \quad (\text{S10})$$

where $S = \sqrt{4e^{2i\phi}\Gamma_1\Gamma_2\beta_1\beta_2 + (2i\Delta - \Gamma_1 + \Gamma_2)^2}$. We observe that for the ideal setup ($\Gamma_1 = \Gamma_2 = \Gamma$, $\beta_1 = \beta_2 = 1$, $\Delta = 0$, $\phi = 2N\pi$) we get $E_{\text{sub}}^R(t) = 0$. This corresponds to the subradiant part of the state $(|e_1, g_2\rangle - |g_1, e_2\rangle)/\sqrt{2}$ being reflected between the two QD forever and never leaving the system while the superradiant part $(|e_1, g_2\rangle + |g_1, e_2\rangle)/\sqrt{2}$ decays with double the decay rate $\Gamma_{\text{sup}}^R = 2\Gamma$. For $\phi = (2N + 1)\pi$ we achieve the identical scenario, just the super- and subradiant states and fields change place. The output fields in the left port can be separated into sub- and superradiant contributions as well:

$$\begin{aligned} E_{\text{sup}}^L(t) &= \frac{-i\sqrt{\Gamma_1\beta_1}(e^{2i\phi}\Gamma_2\beta_2 - i\Delta + (S + \Gamma_1 - \Gamma_2)/2)}{\sqrt{2}S} \exp\left[-(\Gamma_1 + \Gamma_2 + S)\frac{t}{4}\right] \\ E_{\text{sub}}^L(t) &= \frac{i\sqrt{\Gamma_1\beta_1}(e^{2i\phi}\Gamma_2\beta_2 - i\Delta + (-S + \Gamma_1 - \Gamma_2)/2)}{\sqrt{2}S} \exp\left[-(\Gamma_1 + \Gamma_2 - S)\frac{t}{4}\right], \end{aligned} \quad (\text{S11})$$

where the prefactors indicate asymmetry in intensity between the right and left output fields for $\phi \neq 2N\pi$.

The decay rate of the subradiant state becomes finite as soon as only one of the parameters Δ, ϕ deviates from the ideal values above (In case of $\beta < 1$ the subradiant state also decays, but to non-guided "side modes" that do not contribute to the output field so that $E_{\text{sub}}^R(t)$ is still zero.). To lowest order in those parameters the decay rate scales quadratically (assuming for simplicity $\Gamma_1 = \Gamma_2 = \Gamma$ and $\beta_1 = \beta_2 = \beta$),

$$\Gamma_{\text{sub}}^R = \Gamma(1 - \beta) + \Gamma\beta\phi^2/2 + (2 - \phi^2)\Delta^2/(4\Gamma\beta) + \mathcal{O}(\Delta^3/\Gamma^3) + \mathcal{O}(\phi^3), \quad (\text{S12})$$

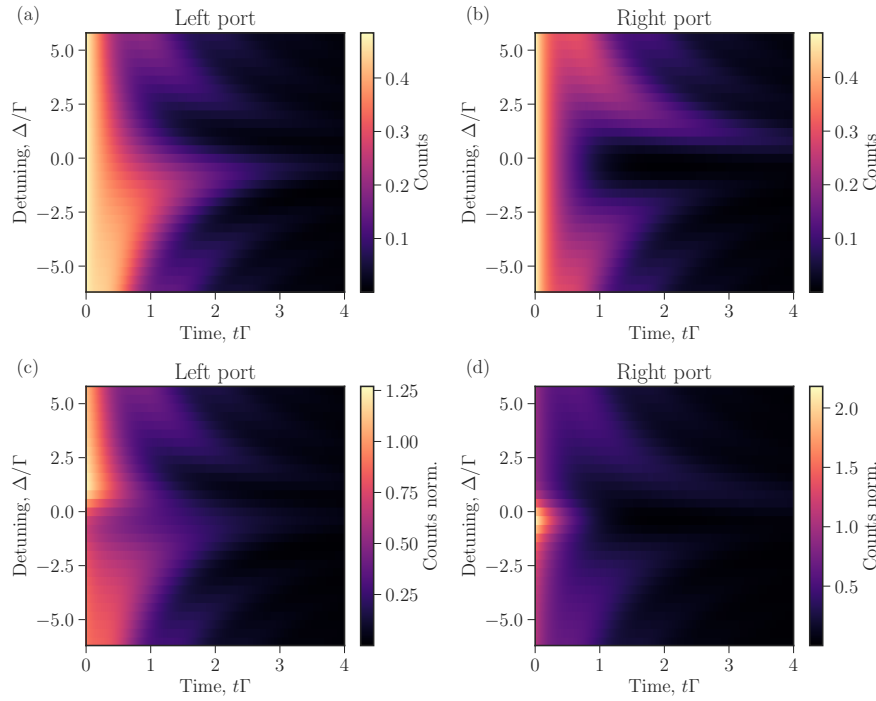


FIG. S3. Increasing the relative phase $\phi_{12} = \pi/4$ acquired between the two QDs leads to asymmetries within and between the left (a,c) and right (b,d) output ports. The absence of asymmetry in the experimental data is a clearly visible indicator for $\phi_{12} \simeq 0$. The normalisation to the sum of each time trace was used for (b,d). The following parameters are assumed: $\phi_{12} = \pi/4$, $\beta_1 = \beta_2 = 0.99$, $\Gamma_1 = \Gamma_2 = \Gamma$, $\gamma_d = 0$.

while the rate Γ_{sup}^R is lowered by the same correction in ϕ, Δ . This manifests in a broad corridor of almost only superradiant decay around $\Delta = 0$, compare the exemplary theoretical study depicted in FIG. S1 qualitatively agreeing with the actual experimental results shown in the main text. The oscillations in intensity for increasing Δ stem from the oscillations between the sub- and superradiant state: in a simplified picture a phase is acquired $|e_1, g_2\rangle + e^{i\Delta t}|g_1, e_2\rangle$ letting both states revolve around the Bloch sphere (FIG. 3) and turn into one another. This is depicted in FIG. S2 for the same theoretically ideal scenario showing an oscillation between the super- and subradiant states $|S\rangle, |s\rangle$. A finite driving time, much shorter than the emitter lifetimes Γ_i is assumed during this calculation. The almost perfect symmetry of the decay tails also indicates a relative phase $\phi \simeq 0$ since this oscillation is corrected in lowest order as $(\Delta + \Gamma\beta\phi)/2$, increasing or decreasing the oscillation frequency depending on the signs of Δ and ϕ , see e.g. FIG. S3.

II. SAMPLE AND OPTICAL SETUP

The sample equivalent to the one described in [S6] is cooled to 4 K in a closed-cycle cryostat with optical access along the z -direction, see FIG. S4. A vector magnet allows to apply an external magnetic field up to 5 T in z direction and 3 T in x -direction. A confocal microscope with 0.8 numerical aperture was used to image the sample, excite the QD from free space, and couple light into the waveguide. A polarisation control is used to reject the laser scattering while collecting the x or y -polarized emission of the collection port 1 and port 2, respectively. Shallow etched gratings [S7] couple to linearly polarized near-gaussian mode and have above 50 nm (FWHM) bandwidth providing a near-equal broadband collection and excitation of the QDs coupled to the waveguide. Details about the sample growth and fabrication can be found in [S6].

Acousto-optic modulators (AOMs) are used to stabilise the optical power of two lasers. The laser used for the resonant excitation of QD optical transitions is continuously tunable between 900-980 nm. A pulsed 5 ps laser is utilized for the excited state lifetime measurements and p-shell excitation. The lasers are combined using non-polarizing beam splitters (BS) to address the photonic chip inside the 4 K cryostat. The polarization for each laser is controlled using polarizing beam splitters (PBS) and a pair of half- ($\lambda/2$) and quarter-waveplates ($\lambda/4$). The emission from the outcoupling grating of the chip is collected using a BS and in case of the p-shell excitation is sent through a spectral filtering setup. The filtering is done using a reflective diffraction grating with 25 GHz FWHM. An avalanche

single photon detector (APD) or superconducting single photon detector (SNSPD) are used to detect the filtered signal depending on the experiment.

In our experiment, the InAs QDs are embedded into the PCW made from a suspended GaAs membrane and connected to grating couplers at each of its ends, to couple light in and out of the PCW (FIG. S4). The intrinsic layer containing self assembled InAs QDs is grown inside the membrane comprising a p-i-n diode. The charge stabilisation allows to achieve near lifetime-limited emission linewidths, while the integration into the PCW leads to near-unity β factor strongly enhancing the photon-emitter interaction $\beta > 98.4\%$ [S8]. This makes it possible to coherently couple emitters separated by distance much longer than the wavelength.

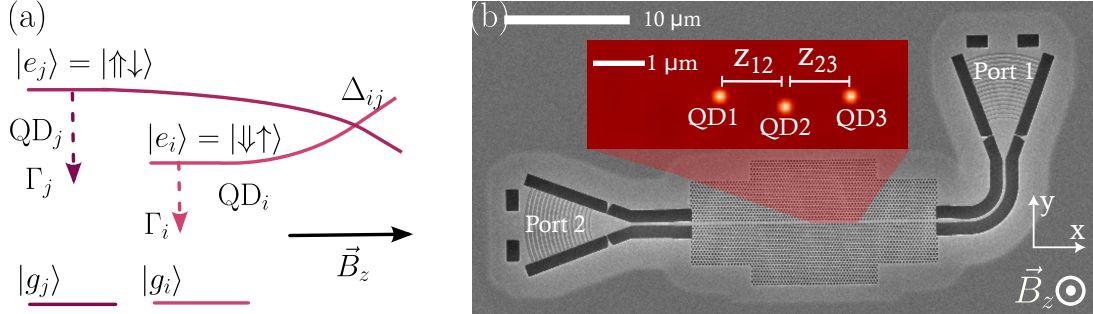


FIG. S4. (color online) (a) Energy level diagram of two QDs detuned by Δ_{ij} and controlled by an external magnetic field B_z . (b) SEM image of the equivalent two-sided photonic crystal waveguide (PCW) structure. The QD is addressed by lasers propagating from free space and the emitted photons are coupled into the waveguide mode, scattered out from right (port 1) or left (port 2) grating couplers and coupled into a single-mode fiber. The inset contains the fluorescence image of the QDs coupled to the PCW (cf. Section IV below).

III. OPTICAL SPECTROSCOPY

FIG. S5 shows the transmission spectra of the PCW and resonant transmission dips of QDs under study with respect to the PCW band edge. This spectra was taken at zero magnetic field and at 1.24V bias voltage.

In FIG. S7 the laser frequency and external magnetic field are scanned. At each laser frequency, laser background correction is performed by normalising to the counts measured at a nonresonant bias voltage of 1 V.

All QDs at zero magnetic field show fine structure splitting (FSS) to be 7.5 GHz (QD1), 6.5 GHz (QD2), 4.1 GHz (QD3). The measured FSS correspond well to the average value for QDs in bulk InAs. QD1 shows strong asymmetry for the two x and y dipoles, where only the high frequency (HF) dipole is well coupled to the PCW, while QD2 and QD3 show a similar coupling also for the low frequency (LF) dipole. These observations are due to the spatial variations of the polarisation of the PCW mode giving different projections of the QD transition dipole moments [S9].

The situation changes once the external magnetic field is applied in the z-direction. Two dipoles are split by the Zeeman interaction and the relative ratio in amplitude between two dipoles is equalised. This is due to the fact that for an out-of-plane magnetic field, the exciton transition dipoles become circularly polarised, and therefore the projection on the local linear PCW polarisation implies that both dipoles couple equally. At high field the Zeeman effect is strongly nonlinear because of the diamagnetic shift equal for all the QDs.

The tuning is done by the out of plane (Faraday geometry) magnetic field (FIG. S7). The external field gives rise to a pair of Zeeman-split energy levels for the excited state $|\uparrow\downarrow\rangle$ and $|\downarrow\uparrow\rangle$ connected to the “empty” ground state $|g\rangle = |0\rangle$, representing two optical dipoles of the QD. The excited state splitting is used to tune the optical transition in resonance with other QDs. The external magnetic field leads to circular polarisations for both dipoles σ_- and σ_+ for $|0\rangle \longleftrightarrow |\uparrow\downarrow\rangle$ and $|0\rangle \longleftrightarrow |\downarrow\uparrow\rangle$, respectively. Using the magnetic field we are able to tune QD2 and QD3 optical transitions in resonance around $B_z = 1.05$ T, QD1 and QD2 close to $B_z = 2.15$ T and QD1 and QD3 at $B_z = 3.4$ T.

The absence of chirality is probed experimentally by comparing amplitudes of resonant transmission dips FIG. S8 for the external magnetic field sweeps in two opposite directions. The ‘mirror’ symmetry around zero magnetic field confirms the assumption of non-chiral interaction.

The fitting of the resonant transmission spectra at zero magnetic field using the theoretical model allows to extract the beta-factor to be above $\beta > 0.8$ for all measured dipoles (TABLE I).

In FIG. S9 the laser frequency and bias voltage are scanned to probe the frequency-voltage map of the QD. At each laser frequency, laser background correction is performed to normalise the counts measured at a non resonant

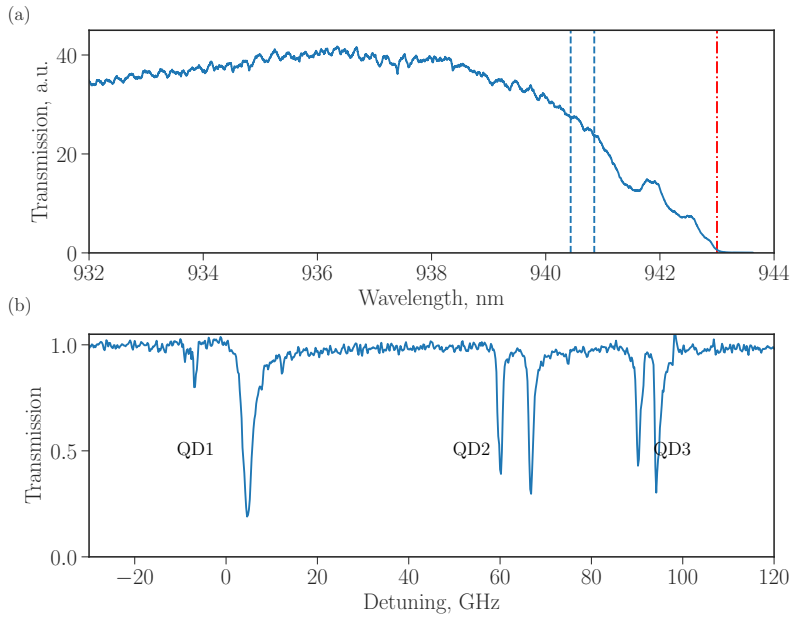


FIG. S5. (color online) (a) Transmission spectrum of the PCW. (b) Transmission spectrum of the PCW at a bias voltage of 1.24 V showing transmission dips of multiple QDs coupled to the optical mode of the PCW. The spectral region containing the QDs under study is indicated between dashed lines centered around 940.55 nm. The band edge of the PCW is estimated to be around 943 nm (dash-dotted line).

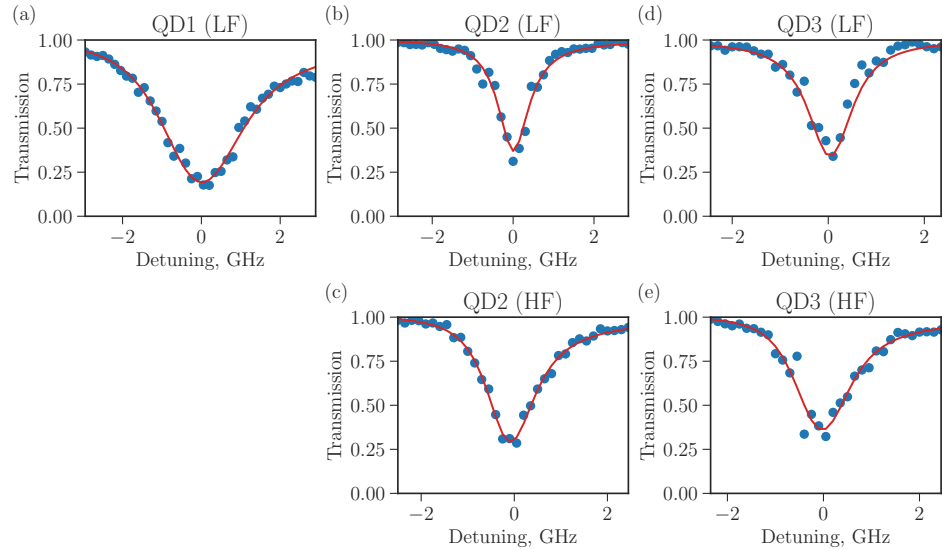


FIG. S6. (color online) Fitting of the resonant transmission spectra for QD1 (a), QD2 (b,c) and QD3 (d,e) for the high frequency (HF) and low frequency (LF) dipoles for each QD at zero magnetic field $B = 0$. For QD1 only the LF dipole is visible at $B = 0$.

bias voltage of 1 V. All QDs show stable excitons between 1.22 V and 1.3 V. The parallel tuning of the two dipoles for each QD confirms the origin of the measured optical lines. If not stated explicitly otherwise, the used voltage for all the measurements presented below was 1.24 V.

TABLE I. Summary of the extracted QD parameters at zero magnetic field: fine structure splitting (FSS), the exciton gyromagnetic ratio (g-factor) g_z , radiative recombination rate Γ , spectral diffusion broadening σ_{sd} .

	QD1	QD2	QD3
FSS, GHz	7.5	6.5	4.1
g_z	1.86	1.91	1.67
$\Gamma/2\pi$, GHz	2.3 (LF)	0.87 (HF), 0.69 (LF)	0.92 (HF), 0.72 (LF)
β	0.94 (LF)	0.88 (HF), 0.83 (LF)	0.84 (HF), 0.83 (LF)
$\sigma_{sd}/2\pi$, GHz	0.59	0.22	0.6

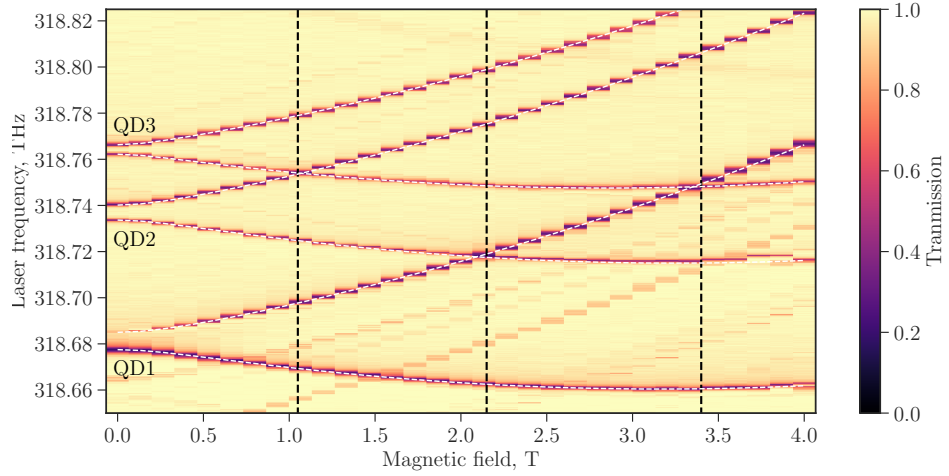


FIG. S7. (color online) The transmission spectrum of the PCW as a function of the out-of-plane external magnetic field B (Faraday configuration). The white dashed lines are the theoretical prediction for the Zeeman effect. The diamagnetic shift σB^2 is estimated to be $\sigma = 2.05$ GHz T $^{-2}$.

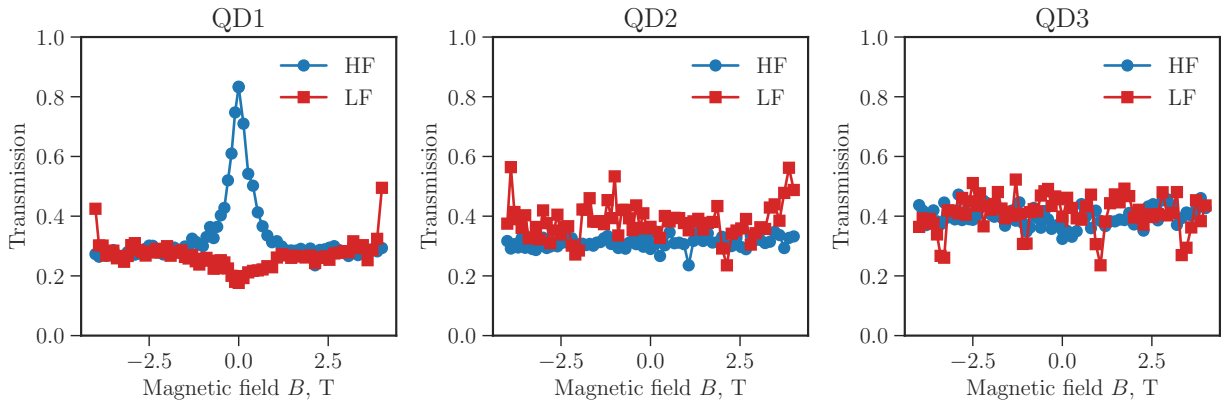


FIG. S8. (color online) Minimum of the transmission spectrum as a function of the magnetic field B for high (HF) and low frequency (LF) dipole for each QD. The symmetry around zero magnetic field illustrates the non-chiral coupling of each QD to the PCW mode.

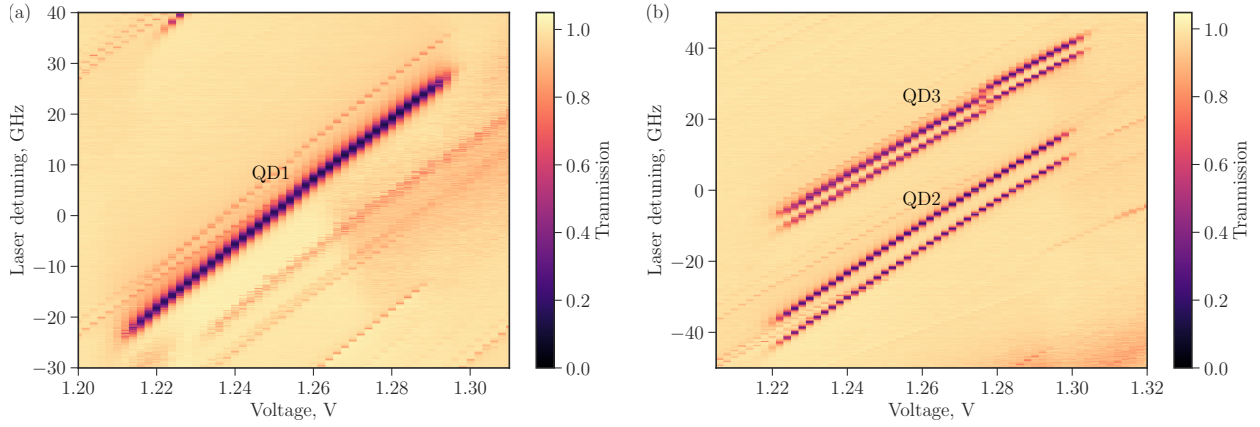


FIG. S9. (color online) The frequency-voltage scan of the resonance transmission for (a) QD1, (b) QD2 and QD3 at zero magnetic field with 318.67 THz (a) and 318.75 THz (b) laser frequency offset.

TABLE II. **Parameters of the photon-mediated coupling for different QD pairs:** radiative recombination rates $\{\Gamma_i, \Gamma_j\}$, spectral diffusion linewidth σ_{sd} , phonon dephasing rate γ_d , phase lag ϕ_{ij} , dissipative coupling rate Γ_{ij} and dispersive coupling rate J_{ij} .

	QD2-QD3	QD1-QD2	QD1-QD3
$\{\Gamma_i, \Gamma_j\}/2\pi$, GHz	0.79, 0.73	0.85, 0.8	0.9, 0.65
$\sigma_{sd}/2\pi$, GHz	0.38	0.18	0.33
$\gamma_d/2\pi$, GHz	0.03	0.03	0.03
ϕ_{ij} , rad	0.05	0.08	0.05
$\Gamma_{ij}/2\pi$, GHz	0.61	0.66	0.61
$J_{ij}/2\pi$, GHz	0.03	0.05	0.03

IV. QD IMAGING

To locate the spatial positions of the QDs within the PCW (FIG.S4) we performed imaging of the sample using a CCD camera. For this six images were taken, one while exciting each QD on and off resonance, respectively. Another image was acquired while imaging the sample surface using broadband light around 940 nm. To excite each QD, the resonant laser light was sent through the PCW (port 1). The CCD camera (DCC CMOS camera (1280 x 1024)) detected the light scattered by the QD outside the PCW mode, for an acquisition time of 30 s. An image of the background (measured at 1 V) was then subtracted, see FIG. S10 (first three images from left). A gaussian fit to the peak was used to identify the position of each QD in pixels, with respect to the camera resolution. The image of the structure, taken with white light on the sample, was used to calibrate the dimensions and extract relative distances.

The position (in pixels) for each QD was found from the Gaussian fit. To calibrate the distance, we used the size of the PCW from the white light image (in pixels) and its size in μm from the mask used to fabricate the chip. We got the ratio between the two units: 181(3) nm/px, leading to the corresponding separations of: 1.25(3) μm for QD1-QD2 (2nd crossing around 2.15 T), 0.96(3) μm for QD2-QD3 (1st crossing around 1.05 T) and 2.21(4) μm for QD1-QD3 (3rd crossing around 3.4 T).

V. ‘OFF-RESONANT’ EXCITATION

To characterise the lifetime of the QDs, ‘off-resonant’ excitation through higher order QD shells (p-shell, d-shell ...) was used. For this a 5 ps 80 MHz pulsed laser was used. The initial characterisation was performed by measuring the excitation spectra of the QD using continuous laser. An example of the excitation spectra for QD2 is shown on

(FIG. S11). The absence of other QD spectral lines in the recorded spectra guaranteed single QD excitation with this method. The excitation frequency was then chosen such that it was far enough from the resonant one, so that it is easier to filter it out of the collection path, but close enough, so that the relaxation time to the s-shell of the conduction band, would not influence the lifetime measurement itself. Specifically, an excitation around 325.72 THz was used for the lifetime measurement (920.4 nm corresponding to one of the peaks in the figure). The power dependence of all three QDs shows the saturation behaviour (FIG. S12). An excitation power close to the saturation was used during the lifetime measurements.

Following the pulsed laser excitation the collected intensity was filtered using an optical grating setup. The intensity was collected from different ports of the PCW (FIG. S5). The lifetime measurement was performed as a function of the external magnetic field around each QD crossing. FIG. S13, FIG. S14 and FIG. S15 show the results of the lifetimes measurements together with the theoretical model, which uses the extracted parameters from TABLE II. The time trace for each magnetic field was normalised to the sum of the total counts in the trace.

The detector response function measured independently was used to fit all the datasets. For QD2-QD3 crossing (FIG. S13) the SNSPD with a 200 ps FWHM temporal jitter was used. While for QD1-QD2 and QD1-QD3 crossings (FIG. S14, FIG. S15) it was a fast APD with 40 ps FWHM temporal jitter.

To find one consistent set of parameters we use the theoretical model described above. Modelling of the data was done by using Eqs. (S10), (S11) to calculate the intensity in each of the ports. Spectral diffusion was taken into account by integrating the overall intensity over the spectral linewidth for detunings Δ between each pair of QDs. Each of the time traces was normalised to the sum of the trace. For fitting, five time traces were used at different detunings around zero detuning. The results of the fit are shown in the TABLE II. $\sqrt{\beta_2\beta_3} = 0.8$ is used during the fitting. This is conservative value leading to a lower bound on the coherent coupling constants that are extracted from the fit.

The extracted coupling constants Γ_{ij} and J_{ij} are very similar for all three QD pairs leading to a similar accumulated phase lag ϕ_{ij} corresponding to predominantly dissipative coupling. This can be explained by the fact that all three QDs were selected using the resonant transmission measurement by giving strong extinction in resonant transmission measurements (FIG. S6). With this approach we pre-select only the QDs that are strongly coupled to the mode of the PCW (i.e. with a high β -factor). Since the β -factor has a strong spatial dependence, this condition results in having QDs at well-defined positions inside the unit cell of the PCW [S10].

Close to the band edge of the PCW the wavevector is given by $ka = \pi$, where a is the lattice constant of the photonic crystal. The phase lag between two QDs separated by the integer number of unit cells $z_{ij} = Na$ is then $\phi_{ij} = N\pi$, corresponding to dissipative coupling. As explained in Section I, under assumption of linear local polarization inside the PCW mode the effects from the directional chiral coupling can be ignored. The effects from local phases due to QDs positioned off-axis in the PCW can be incorporated into the definition of the phase ϕ , while keeping the same definition for the coupling constants Eq. (S5).

We notice that the separations between QD pairs are very close to the integer number of unit cells of the photonic crystal with period $a = 240$ nm: $z_{12} = 5.2(1)a$, $z_{23} = 4.0(1)a$ and $z_{13} = 9.2(2)a$. This leads to similar contributions from dissipative Γ_{ij} and dispersive J_{ij} coupling for different QD pairs.

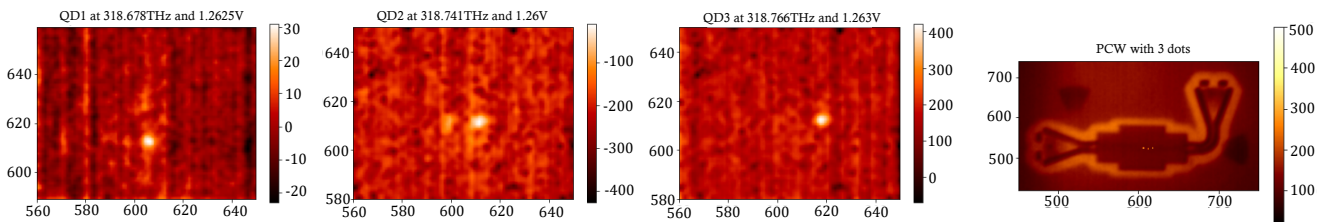


FIG. S10. Imaging of QD1, QD2 and QD3 in the PCW. The first three (from left) images were taken during resonant transmission measurements and were fitted accordingly to extract the maximum of the counts, revealing each QD position. The fourth image is done using broadband light centered around 940 nm illuminating the chip. The image is superimposed with first three images. The frequency and bias voltage used for each QD are noted. The axes units are in pixels.

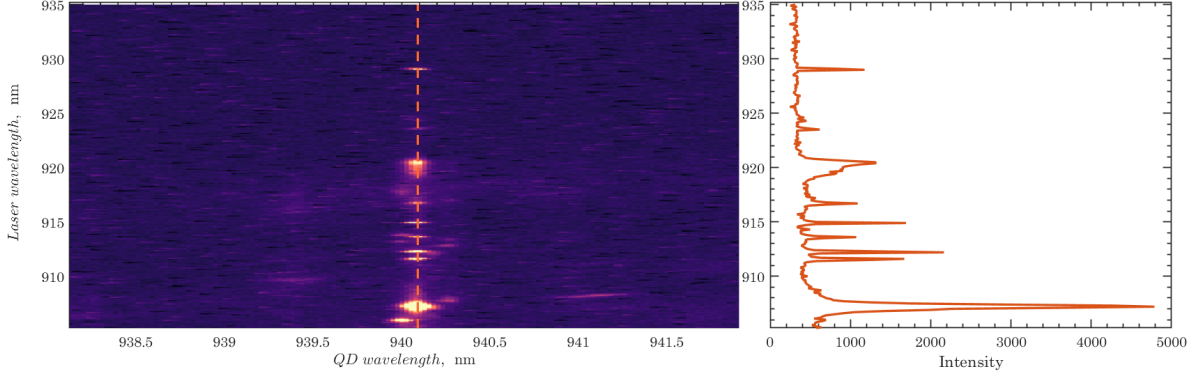


FIG. S11. Example of the excitation spectra of QD2 at zero magnetic field emitting at 940.09 nm (dashed line). The 2D map on the left side shows higher energy level states of QD2 while the frequency of the continuous excitation laser is increasing. The excitation around 920.4 nm was used for lifetime measurements. The plot on the right shows a photoluminescence excitation spectra recorded at a fixed wavelength of 940.09 nm (dashed line in the left plot).

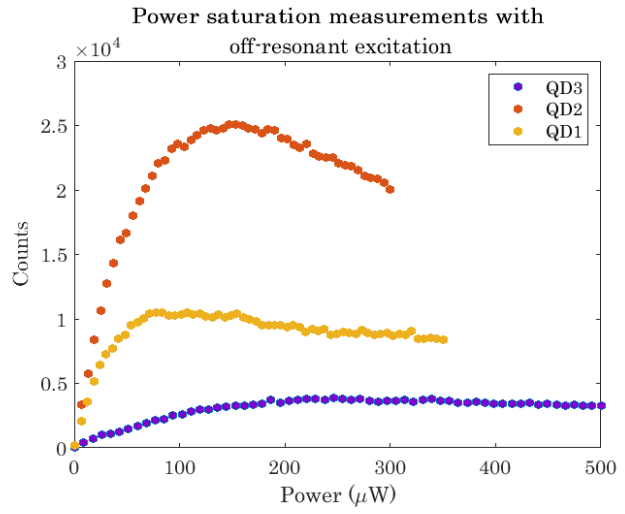


FIG. S12. Power saturation measurements for the three QDs, when driven by a pulsed off-resonant excitation beam.

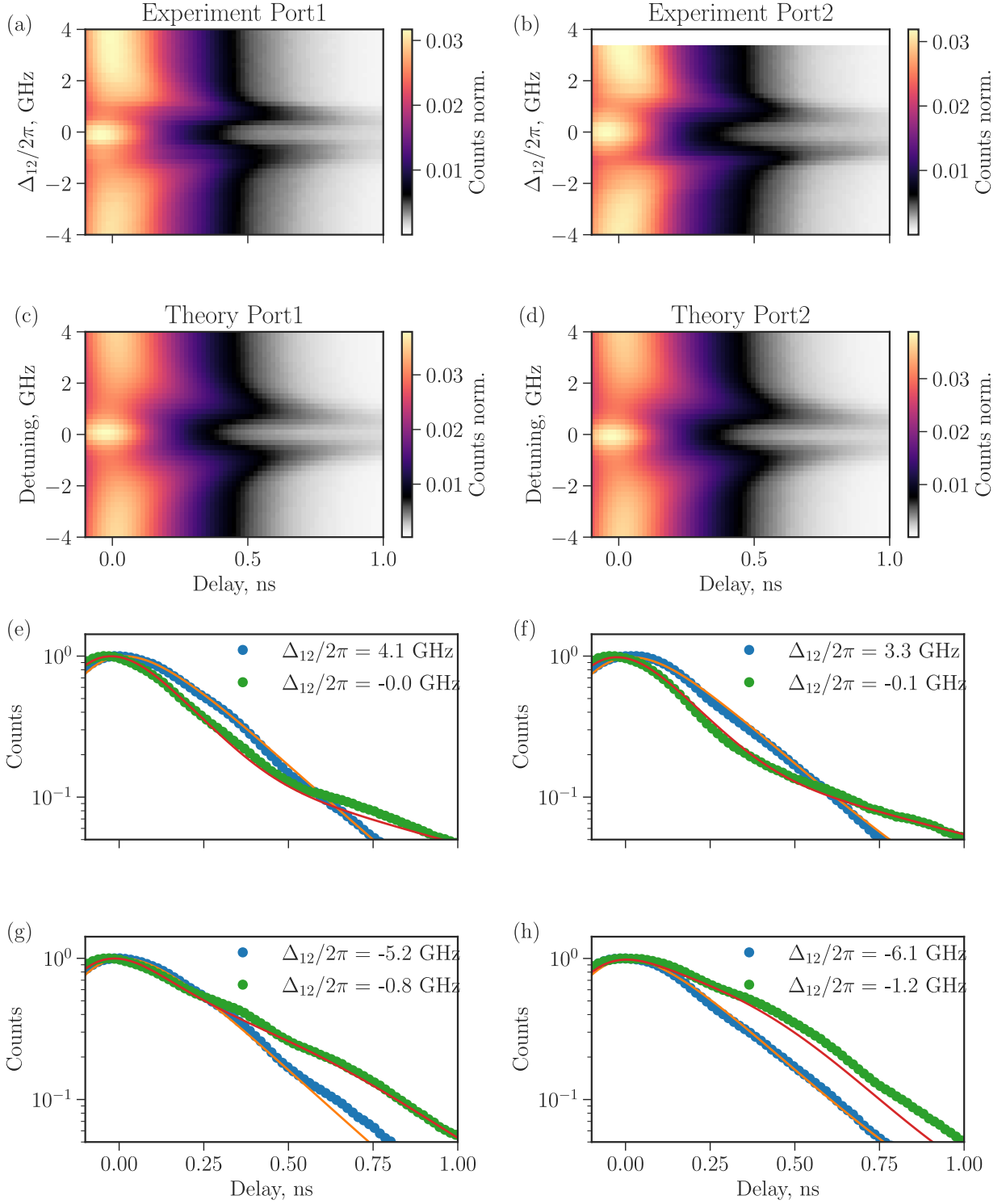


FIG. S13. (color online) 'Off-resonant' excitation of QD2 for different detunings from QD1 and at a magnetic field of 2.1 T. (a-b) Experimental decay dynamics of QD2 as a function of the detuning between QD1 and QD2 Δ_{12} for photon collected from port1 (a) and port2 (b). (c-d) Theoretical calculation represented by the developed theory model. (e-h) Decay dynamics for different frequency detunings between QD1 and QD2 Δ_{12} . For off resonant condition the decay is fitted using two decay processes, where the 2nd decay rate is equal to 0.07(1) GHz, associated with a spin-flip process. The on resonance decay consists of two decay processes corresponding to the super- and subradiant decays. The decay with detuning close to the linewidth (green dots) contains additional modulation on top of the decay. Parameters from TABLE II were used for theory curves.

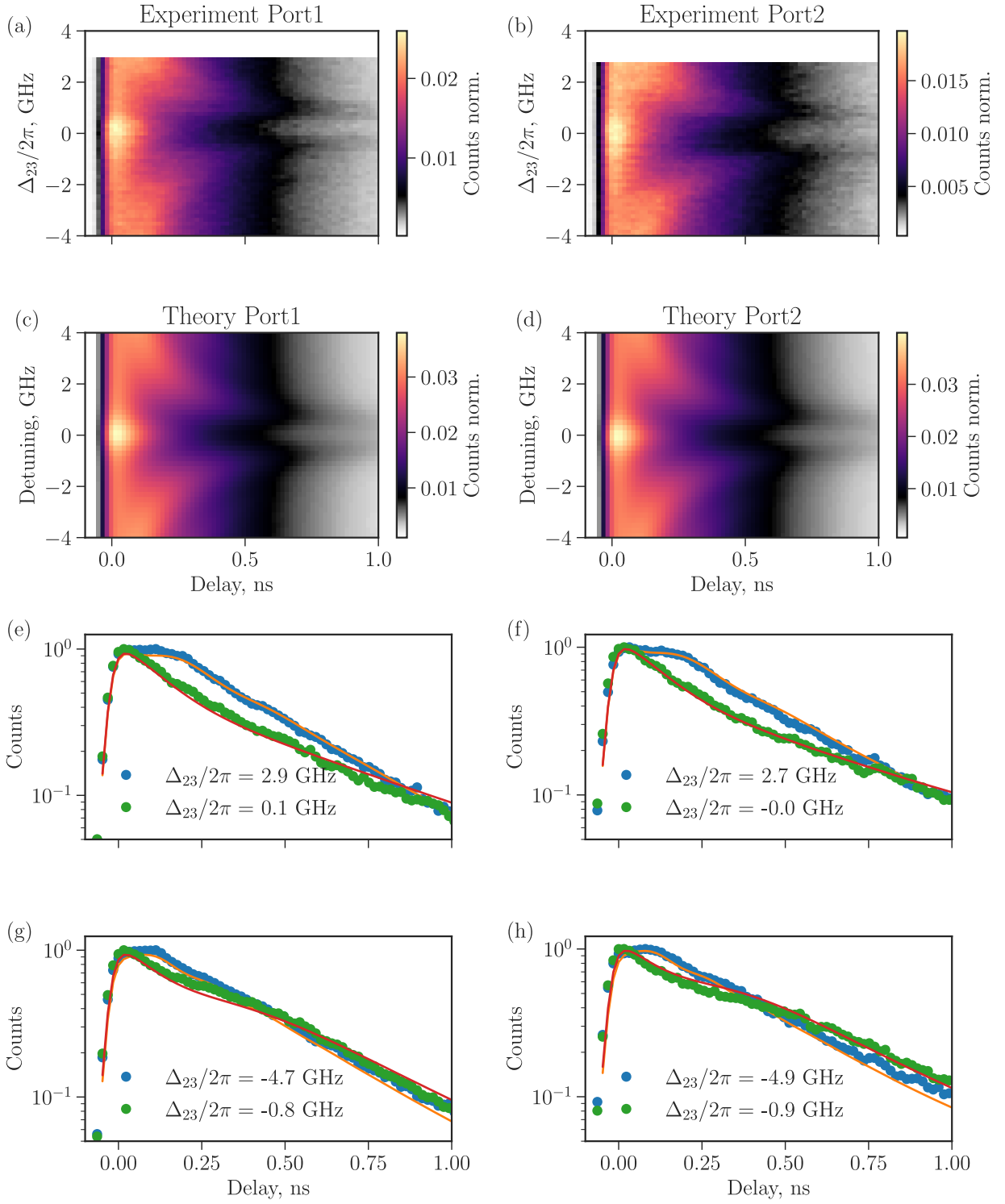


FIG. S14. (color online) Same as Fig. S13 but for excitation of QD3 and varying the detuning to QD2 and at a magnetic field strength of 1.0T.

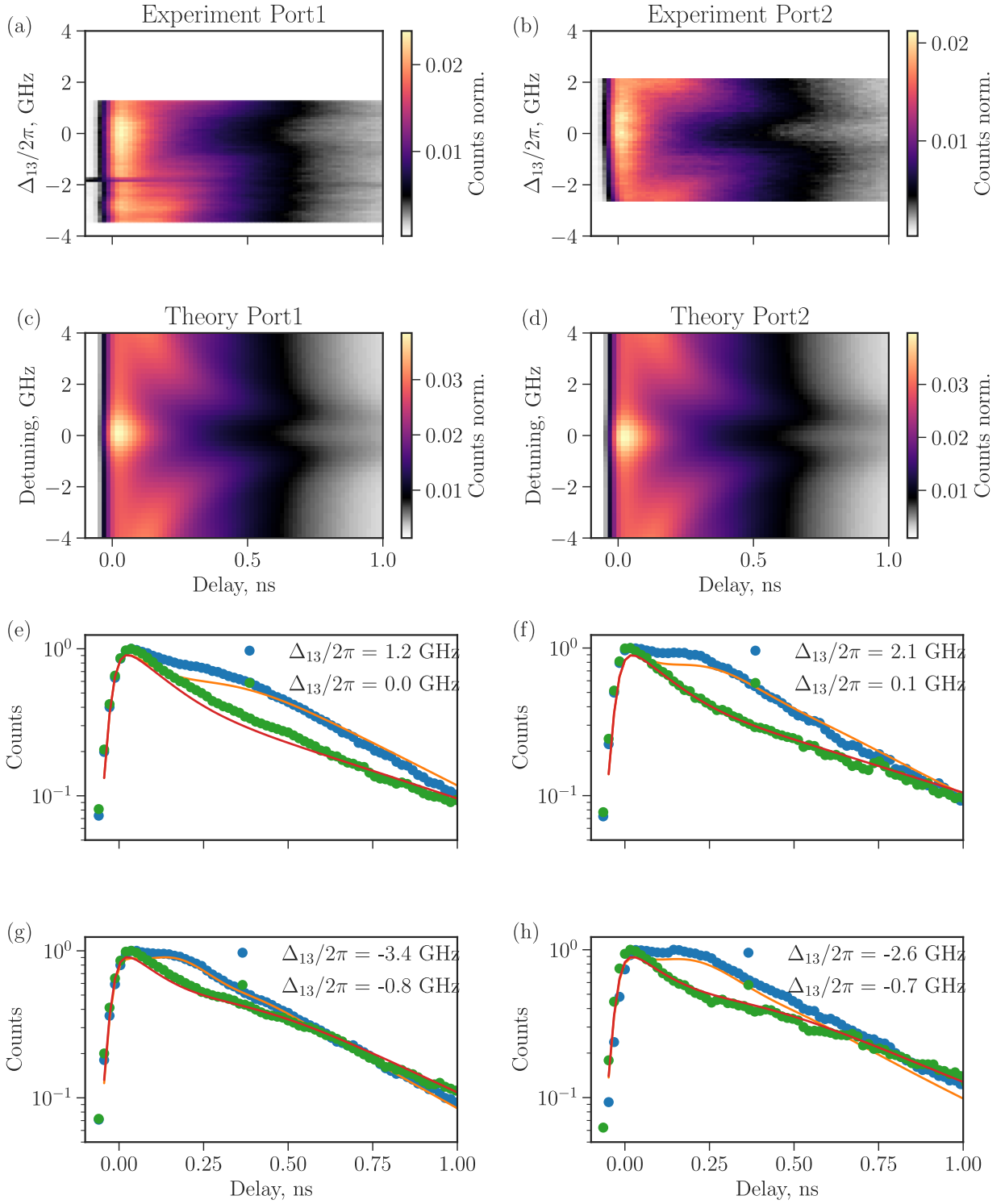


FIG. S15. (color online) Same as Fig. S13 but for excitation of QD1 and varying the detuning to QD3 and at a magnetic field strength of 3.5T.

TABLE III. **Parameters of the photon-mediated coupling for QD2-QD3 pair while driving both QDs:** radiative recombination rates $\{\Gamma_2, \Gamma_3\}$, spectral diffusion linewidth σ_{sd} , phonon dephasing rate γ_d , phase lag ϕ_{23} , dissipative coupling rate Γ_{23} and dispersive coupling rate J_{23} , Ω_2 , Ω_3 excitation pulse areas, θ phase between two driving fields.

$\{\Gamma_2, \Gamma_3\}/2\pi$, GHz	0.79, 0.73
$\sigma_{sd}/2\pi$, GHz	0.38
$\gamma_d/2\pi$, GHz	0.03
ϕ_{23} , rad	0.05
$\Gamma_{23}/2\pi$, GHz	0.61
$J_{23}/2\pi$, GHz	0.03
Ω_2, Ω_3	0.87(6), 1.33(5)
θ	$-0.48(2)\pi$

VI. RESONANT EXCITATION

The dynamics shown in FIG. 2(d) and FIG. 3(c) in the main text are induced by resonant (s-shell) excitation. In this case the pulsed laser frequency was tuned into resonance with the emission frequency of the driven QDs, i.e. about 318.76 THz. The laser was suppressed in the collection path with both a transmission grating and a temperature-controlled etalon filter, where the latter has a narrow linewidth of 3 GHz. The excitation pulse from the laser was stabilized with an AOM and frequency filtered. The power for the laser pulse was calibrated based on Rabi oscillations with the QDs off-resonant from each other (FIG. S16).

Results of the excitation of QD3 when tuned close to resonance with QD2 are shown on FIG. S17. The recorded behaviour is equivalent to the measurement results with 'off-resonant' excitation.

The difference becomes clear when exciting both QDs from the pair, see FIG. S18. For these measurements, the same setup is used by while the polarisation of the driving laser field is adjusted to pump both QDs. The phase difference between two excitation fields is $\theta \approx \pi/2$ which is set by the local polarisation projection of the driving field to two dipoles of the crossing. The two QD transition dipole moments are orthogonally (circularly) polarized in the Faraday magnetic field configuration, see FIG. S5a., corresponding to the transitions $|0\rangle \longleftrightarrow |\uparrow\downarrow\rangle$ and $|0\rangle \longleftrightarrow |\downarrow\uparrow\rangle$, respectively. The polarisation control of the driving field allows to effectively control the phase θ between two driving fields.

The fitting of the phase θ and driving field areas Ω_1 and Ω_2 was done using the theoretical model described above. The parameters extracted from the previous fit TABLE II for QD2-QD3 pair were used, while fitting only θ , Ω_1 and Ω_2 parameters. The results are given in the TABLE III.

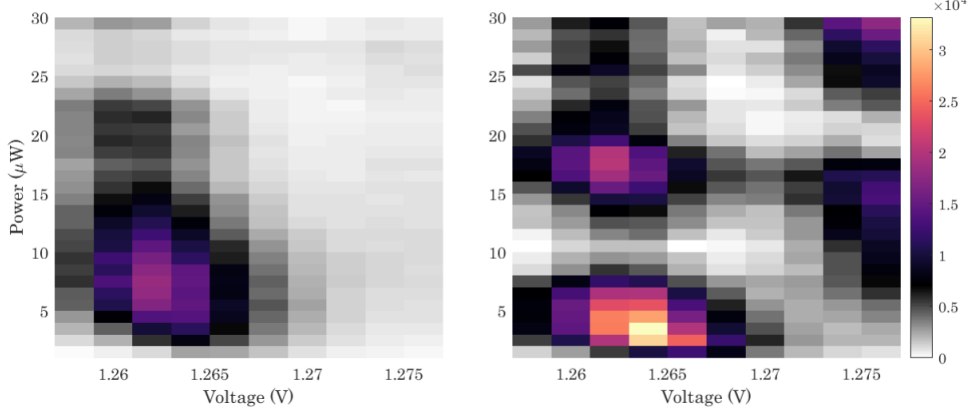


FIG. S16. **Saturation curves showing Rabi oscillations.** Left: Exciting only one dipole (QD3) of the QD2-QD3 pair. Right: Exciting both dipoles after rotating the polarisation of the excitation laser. The dipole of QD2 is in resonant with the filtering etalon when applying a voltage around 1.277 V. Maxima appear for two different values of the bias voltage, indicating that both dipoles are populated for different powers. The measurement is done at magnetic field of 0.8 T, using 5 ps laser centered around 940.5 nm.

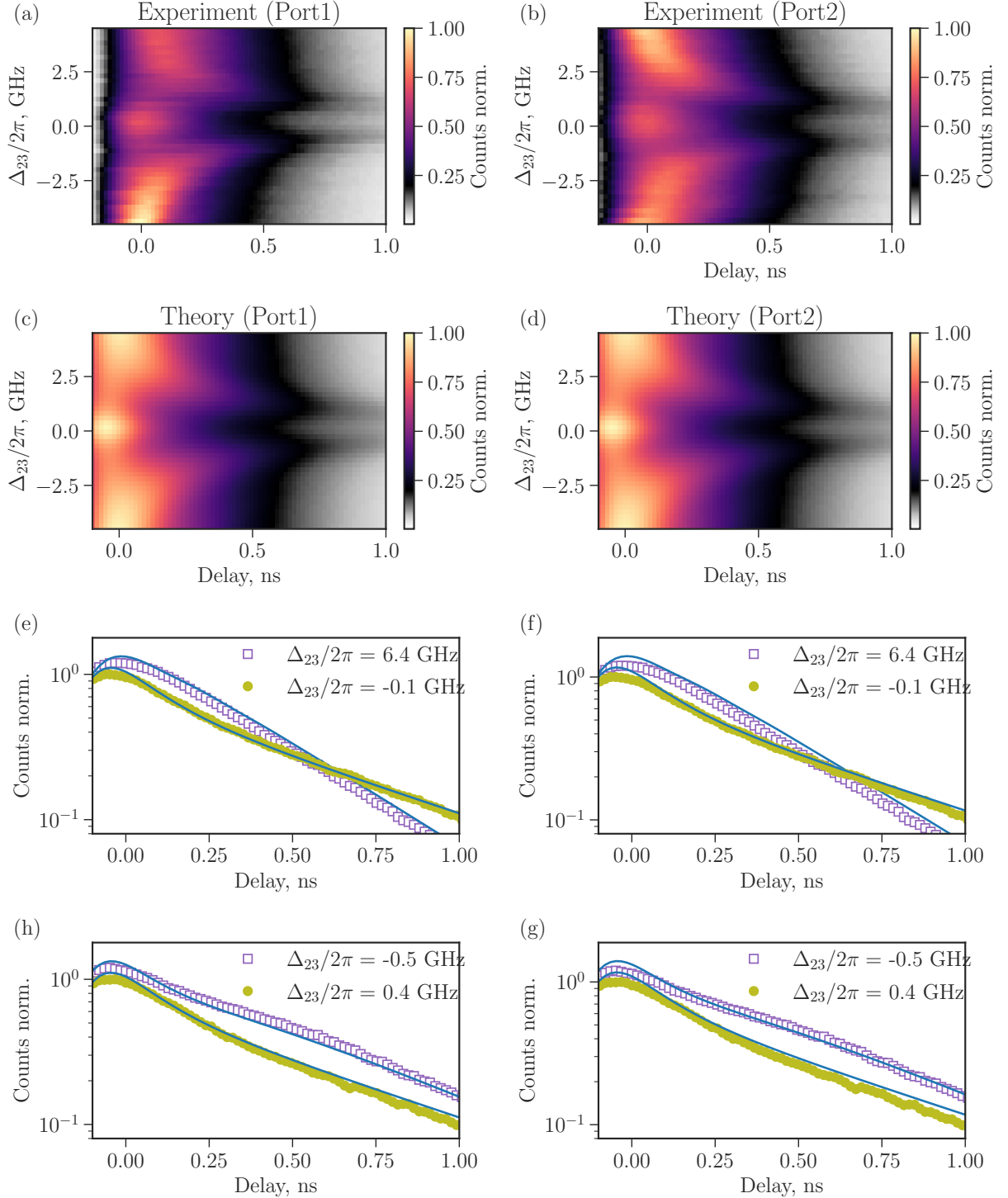


FIG. S17. (color online) Resonant excitation of QD3 around the resonance with QD2 at 1.05 T. (a-b) The experimental excitation dynamics of QD3 as a function of the detuning between QD2 and QD3 Δ_{23} for photon collected from port1 (a) and port2 (b). (c-d) Theoretical calculation represented by the developed theory model. (e-h) Decay dynamics for different frequency detunings between QD2 and QD3 Δ_{23} . The on-resonance decay consists of two decay processes corresponding to the super- and subradiant decays. For the detuned case an additional coherent modulation is superposed on top of the decay. Parameters from TABLE II were used for theory curves.

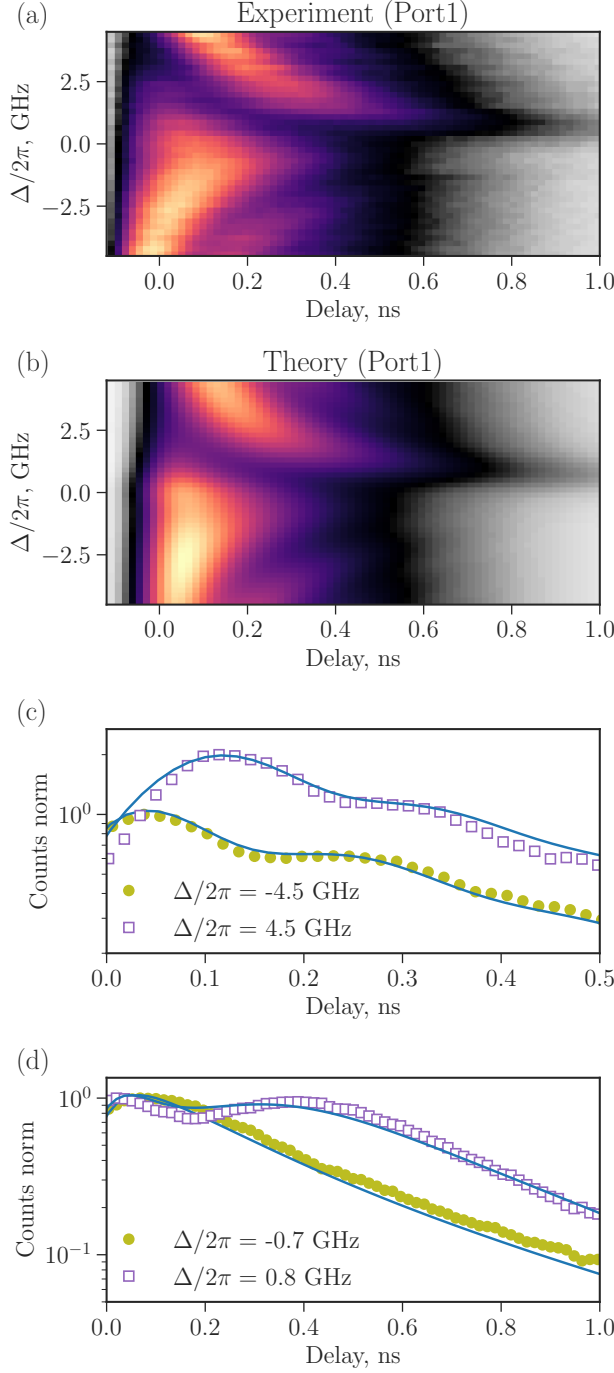


FIG. S18. (color online) Resonant excitation of the QD2-QD3 pair around their resonance at 1.05 T. (a) Experimental excitation dynamics of the QD2-QD3 pair as a function of the detuning between QD2 and QD3 Δ_{23} for photons collected from the port1. (b) Theoretical calculation represented by the developed theory model. (c-d) Decay dynamics for different frequency detunings between QD2 and QD3 Δ_{23} . Parameters from TABLE III were used for theory curves.

- [S1] P. Lodahl, S. Mahmoodian, S. Stobbe, A. Rauschenbeutel, P. Schneeweiss, J. Volz, H. Pichler, and P. Zoller, *Nature* **541**, 473 (2017).
- [S2] H. T. Dung, L. Knöll, and D.-G. Welsch, *Phys. Rev. A* **66**, 063810 (2002).
- [S3] A. Asenjo-Garcia, M. Moreno-Cardoner, A. Albrecht, H. J. Kimble, and D. E. Chang, *Phys. Rev. X* **7**, 031024 (2017).
- [S4] A. Albrecht, L. Henriet, A. Asenjo-Garcia, P. B. Dieterle, O. Painter, and D. E. Chang, *New Journal of Physics* **21**, 025003 (2019).
- [S5] D. E. Chang, A. S. Sørensen, E. A. Demler, and M. D. Lukin, *Nature Physics* **3**, 807 (2007).
- [S6] R. Uppu, F. T. Pedersen, Y. Wang, C. T. Olesen, C. Papon, X. Zhou, L. Midolo, S. Scholz, A. D. Wieck, A. Ludwig, and P. Lodahl, *Science Advances* **6**, eabc8268 (2020).
- [S7] X. Zhou, I. Kulkova, T. Lund-Hansen, S. L. Hansen, P. Lodahl, and L. Midolo, *Applied Physics Letters* **113**, 251103 (2018).
- [S8] M. Arcari, I. Söllner, A. Javadi, S. Lindskov Hansen, S. Mahmoodian, J. Liu, H. Thyrrstrup, E. H. Lee, J. D. Song, S. Stobbe, and P. Lodahl, *Phys. Rev. Lett.* **113**, 093603 (2014).
- [S9] P. Lodahl, S. Mahmoodian, and S. Stobbe, *Rev. Mod. Phys.* **87**, 347 (2015).
- [S10] A. Javadi, S. Mahmoodian, I. Söllner, and P. Lodahl, *J. Opt. Soc. Am. B* **35**, 514 (2018)